2009-02-11

Source Localization via Near Field Signal Processing

Vivek C. Varshney
Worcester Polytechnic Institute

Source Localization via Near Field Signal Processing

by

Vivek C. Varshney

A Thesis
Submitted to the Faculty
of the
WORCESTER POLYTECHNIC INSTITUTE
in partial fulfillment of the requirements for the
Degree of Master of Science
in
Electrical and Computer Engineering
by

February 2009

APPROVED:

Professor David Cyganski, Major Advisor

Professor R. James Duckworth

Professor Arthur Heinricher

Abstract

This thesis is in support of the Precision Personnel Locator (PPL) project being conducted by Worcester Polytechnic Institute (WPI). The overall goal of the PPL project is to locate firemen and other emergency personnel in buildings using Radio Frequency (RF) techniques. The aspiration is to prevent a tragedy similar to the Worcester Cold Storage fire of 1999.

The Mantenna homing wand is a spinoff of the PPL system which uses the Near Field properties of Very Low Frequency (VLF band) waves. The Mantenna has been used to successfully demonstrate the ability to locate targets inside harsh RF environments and other radio opaque environments where normal radiation field based systems have degraded performance, such as commercial, industrial, and apartment buildings.

This thesis builds upon the Mantenna rescue device by construction of a transmitter subsystem which is physically smaller than the previous version by redesign of the compact VLF antenna. Additionally, exploitation of the approach used by the Mantenna for homing purposes is explored for full location estimation. This work provides the theoretical background and proof of concept test of a Near Field based location system. Simulation and test results are compared for a minimal configuration involving a single receiver.

Acknowledgments

I would like to thank the members of the Machine Vision Laboratory (MVL) at WPI. In particular, the past Mantenna Research Assistants, Chung Yun "Jason" Huang and Jason Farmer, for their initial work to prove the Near Field concepts and initial development of the Mantenna rescue device.

I would also like to thank all the PPL project members for their ideas and suggestions which helped make life as a graduate student more enjoyable. A special thanks to Bob Boisse for helping build hardware and availability to help with field tests.

I would also like to thank the members of the Worcester Fire Department for always providing feedback and suggestions to help improve upon our work. In addition, their willingness to allow us to use their burn building as a testing ground forced us to bring out the best the technology can offer.

I would also like to thank my thesis committee for taking time out of their busy schedules to provide advice and suggestions to improve the research developed in this thesis.

In addition, I would like to thank Professor David Cyganski of the ECE Department for his help, guidance, and patience during this project. Without his insight, this life saving device would not be possible.

Contents

List of Tables

List of Figures

Chapter 1

Introduction

The Mantenna project is being developed as a spinoff of technology originally developed by the Precision Personnel Locator (PPL) team in the Electrical and Computer Engineering (ECE) Department of Worcester Polytechnic Institute (WPI). This project is funded by the Department of Justice's (DOJ) National Institute of Justice (NIJ).

The goal of this project is to develop a rescue system to locate trapped first responders in harsh Radio Frequency (RF) environments where the PPL system may have severely degraded performance. The Mantenna differs from the PPL system in that the Mantenna is a homing system rescue device which uses the Near Field property of Very Low Frequency (VLF) band waves, while the PPL system is a position and tracking rescue system using the radiation far field of Ultra High Frequency (UHF) band waves.

This thesis describes work in support of the Mantenna project by first summarizing the development of an improved antenna design for the Mantenna transmitter and receiver. This thesis then explores the theoretical background and a proof of concept demonstration of a Near Field based tracking and rescue system.

1.1 Motivation for the Project

On December 3, 1999 a tragedy struck the northeastern part of the United States as six firefighters lost their lives. An abandoned brick building, the Worcester Cold Storage and Warehouse Co. building, became a inferno as the building was host to a raging fire. Initially, two firefighters entered the building looking for a homeless couple who were thought to be trapped inside. The two rescuers soon became lost and disoriented due to the thick smoke and heat, and radioed for help. Two more teams of two firefighters went

in to locate the disoriented pair, but both teams also became disoriented and lost. After some time, the fire was too fierce and the commander ordered all firefighters to evacuate the building, however the above six did not make it out. Several days later the six men were found dead inside the remains of the building less than 100 feet from an exit [1].

The Worcester Cold Storage and Warehouse Co. building was an abandoned industrial building from the city of Worcester's industrial heyday. It was constructed as a giant cold storage (refrigerated) building for storage of meat and other materials, as household refrigerators were not common during the era of construction. This windowless building had walls nearly 18 inches thick which were coated in petroleum based insulation, a common method of insulating buildings during that period. During their use, the industrial equipment and machinery were cooled using petroleum based coolants, which inevitably seeped into the floors and walls. These facts would render nearly every former industrial building a raging inferno, similar to the Worcester Cold Storage and Warehouse Co. fire, should they ever catch fire [2].

Abandoned industrial buildings, such as the aforementioned Cold Storage building, and other mill buildings, are very common in present day Worcester. During their period of use, these industrial buildings were often reconfigured and expanded, and being configured in an era prior to one in which floor plans were given to the city, the layout of the present configuration of each building is unknown. The Cold Storage building lacked windows above the second story, making it difficult for the firefighters to judge their position in the building. During the search for the missing firemen, parts of the building walls were breached, along with an elevator-shaft roof skylight, which, combined with the petroleum coated interior, had the unfortunate effect of turning the building into a giant inferno [2].

When the industrial jobs occupying those buildings moved away, the buildings became vacant. Most buildings were not razed or sold, as the companies which occupied them simply vanished, and the City and State did not have the funds to demolish them. The buildings, eventually abandoned and decrepit, became occupied by the homeless.

The WPI Precision Personnel Locator project seeks to find a Radio Frequency (RF) based approach to locate the whereabouts of personnel inside of a building, with the goal of preventing another tragedy such as the Worcester Cold Storage fire. The goal of the WPI team is to create a system that is easy to operate, does not require any pre-existing building infrastructure, and can perform well in harsh environments (tough physical and RF environments) [3]. In addition, the system must be usable the moment the firefighters

step off of firetrucks and must function without any knowledge of the building layout.

This work seeks to use a Near Field RF based system to accomplish these goals in harsh RF environments where the PPL system fails. Initial research showed that a Near Field approach had enough merit that the project was spun off into the Mantenna Project despite the decision to concentrate location and tracking research on a far field approach. Thus, while the PPL Project uses high frequency RF to locate a firefighter for tracking and rescue purposes, the Mantenna Project uses Low Frequency (LF) RF for rescue only. The Mantenna is essentially an RF homing wand, such that when a firefighter is in trouble an RF signal is transmitted by a device worn by the firefighter, and the Mantenna receiver carried by the rescuer can be used to locate him/her. Due to the properties of near field waves, combined with the use of a low frequency, the Mantenna is able to penetrate sheets of metal and work in harsh RF environments as described in Section 2.2 with a range on the order of 50 to 100 feet.

The Mantenna System, Version 3, is shown in Fig. 1.1. The Mantenna Receiver Wand, Version 3, is depicted in Fig. 1.1(a). The Mantenna Transmitter System, Version 3, is depicted in Fig. 1.1(b). The Mantenna concept of operation is that each firefighter would carry a Mantenna Transmitter System which contains the antenna and electronics. The radio should either be closely coupled to or integrated with the Personal Alert Safety System (PASS) device. When a firefighter is in distress, the PASS device should activate the Mantenna Transmitter System, with the idea being that the rescue personnel using a Mantenna Receiver Wand would be able to locate the firefighter in distress. A rescuer continuously sweeps the receiver wand from left to right and up and down to determine the direction producing the strongest indicator response from the unit and proceeds in that direction towards the distressed firefighter. The indication given by the receiver wand is: an audio tone, whose pitch increases with decreasing distance from the transmitter and with improved aim towards it; a LED bar graph with increasing intensity linked to the increasing audio pitch; and a vibration of the unit which too increases in frequency as does the audio tone. As the rescuer gets closer to the transmitter, the indication will become stronger until the audio tone, LED indicator, and vibration start pulsing; at this distance, the distressed firefighter is within arms reach of the rescuer.

(a) Mantenna V3 Receiver Wand

(b) Mantenna V3 Transmitter

Figure 1.1: Mantenna System Version 3

1.2 Mantenna and Near Field Locator System Requirements

Based upon discussions and experience with the Worcester Fire Department and tempered by the capabilities expected from a Near Field homing system as seen in initial concept explorations, it was determined that a Mantenna system should meet the following requirements:

- Must bring rescuer to < 1 meter away from person in distress
- Must have minimum range of 50 feet
- Must require minimal training to operate
- Must be easy and intuitive to operate
- Must work in harsh RF environments
- Target cost of $< \$1,000$ per system
- Transmitter must transmit location signal for several hours, in case access to person in distress is delayed
- Transmitter must be small and light enough to carry on SCBA
- Receiver wand portion must be small and light enough to be carried easily
- Must be ruggedized, waterproof, fire-resistant and durable

With these goals in mind the Mantenna system was developed with contributions from a succession of graduate Research Assistants. In the Near Field Locator Project, we have chosen to continue adherence to these same general requirements.

1.3 Path to the Near Field Locator Concept

During the infancy of the PPL project, the WPI team investigated several possible precision location and tracking approaches. A summary of some of the researched approaches is listed below.

Currently when the firefighter is in distress, their PASS Device will sound a loud audio alert. Distress includes being low on air, no motion for thirty seconds, or any other condition that might induce the firefighter to activate a panic button. The hope is that a nearby firefighter will hear the sound and be able to locate the person in distress. By talking to the Worcester Fire Department, the PPL team learned this device's operation is known to fall short of their needs, since the audio alert isn't always audible during a fire due to the mask and breathing apparatus worn by the firefighter and the intense noise of the fire [2].

The existing Global Positioning System (GPS) uses UHF signals RF from satellites orbiting in space to essentially triangulate signal delays and estimate the position of the GPS receiver on the surface of the earth. However, GPS has two flaws that make it impossible to use for the PPL project, the first being that outdoor accuracy does not meet the desired 1 meter accuracy, the second being that weak signal penetration of buildings and multipath interference severely degrade operation [4]. The accuracy of the civilian GPS system while outdoors is at best approximately 10 meters, which is fine for most civilian uses, but not as accurate as needed by the PPL application.

Another approach investigated was based upon inertial sensors. These sensors report the acceleration experienced in X, Y, and Z directions. Upon examination, it was discovered that low cost sensors drift to an unacceptable degree, and sensors with an acceptable drift allowing accurate location over a span of several minutes are prohibitively expensive.

Another approach investigated was the Avalanche Beacons used by skiers. The idea behind Avalanche Beacons is all skiers carry a transmitter and if they are trapped by an avalanche, a rescue team with a receiver can home in on them. The transmitter only transmits along one axis, so a rescuer's received signal is highly dependent upon the

orientation of the transmitter. Additionally, the system was found to work poorly in high multipath environments [5] [6].

The PPL team decided to use an RF based approach, using the radiation far field of electromagnetic waves. The idea is that each firefighter inside a building would wear a transmitter transmitting the location signal. Fire trucks with arrays of antennas would surround the building and receive the signal, then signal processing would be performed to determine the firefighter's position and the results displayed on the commander's screen.

A major problem with any radiation far field based approach is multipath interference. This interference is caused by the transmitted signal being reflected by various metallic items in the environment and these reflections contributing to the received signal, as shown by Fig. 1.2. The PPL team developed an impressive algorithm to help mitigate, but not eliminate, the effects of multipath, as is described in Vincent Amendolare's Masters Thesis [7].

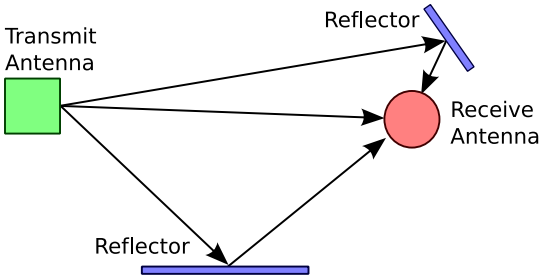

Figure 1.2: Multipath Interference

During the development of the Mantenna, it was shown that the Near Field (Coulomb Field and Induction Field) did not significantly suffer from multipath interference. The Mantenna rescue system works nearly flawlessly in buildings where multipath is so prevalent that the full PPL system fails. Because the Mantenna technology works in extremely harsh RF environments, it was decided to explore Mantenna technology as a tracking and rescue system, with the hope it succeeds in environments where the prior system fails.

1.4 Precision Personnel Locator System

The PPL system differs from the Mantenna system in that the Mantenna is a rescue device while the PPL is a tracking and rescue device. Using the PPL system, a firefighter will arrive on scene wearing a PPL transmitter. In the PPL system, the transmitter

is always transmitting the RF positioning signal. Additionally, antennas are retrofitted onto fire trucks, and adequate coverage is attained by having many fire trucks surround a building. The antennas on the trucks receive the firefighter's signal, then send this data to the commander's vehicle. The commander's vehicle performs the necessary signal processing to obtain a position estimate, then displays the results on a screen for the Incident Commander (or Chief) to view.

With the PPL system, the Incident Commander (or Chief) is able to view the location of several firefighters in real-time on a laptop display. In addition, the PPL system allows viewing the path any firefighter took to get to their current position, a feature which could be helpful in directing rescue personnel to a distressed firefighter. The display also reports vital signs of the personnel, such as heart rate, respiration, orientation, etc., and alerts the viewer if any personnel are thought to be in distress. An example of such a display is seen in Fig. 1.3.

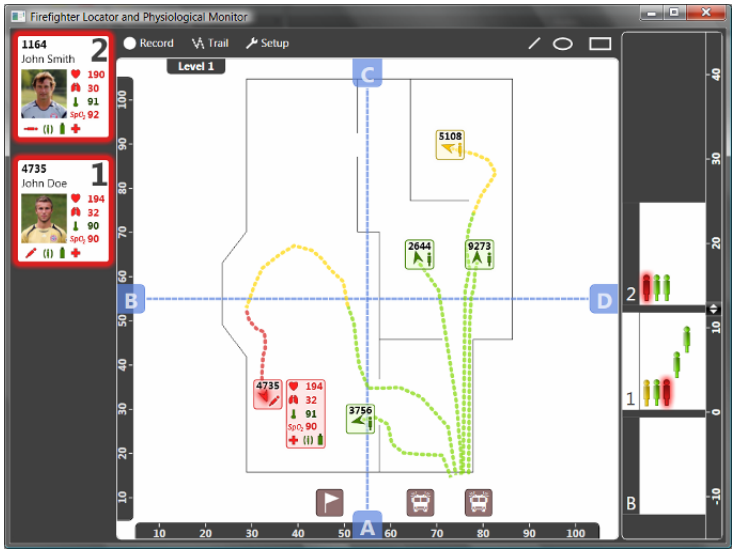

Figure 1.3: Example Display for Incident Commander, PPL System

In an emergency, the rescuer must be directed by the Incident Commander to the distressed firefighter, since each firefighter is wearing a PPL transmitter and not carrying any receivers. The Incident Commander can view the path traversed by the distressed firefighter and use that information to help direct which way the rescuer should travel. This system requires training of personnel in order to use the system to its full extent.

1.5 Mantenna Homing System

The Mantenna Homing rescue system consists of two parts, the transmitter system (antenna and associated electronics) and the receiver wand. The Mantenna is a small, low cost (under $1,000), short range device that uses the near field for high penetration of building materials and requires little training and no setup time to use. The Mantenna Receiver Wand and Transmitter are seen in Fig. 1.4.

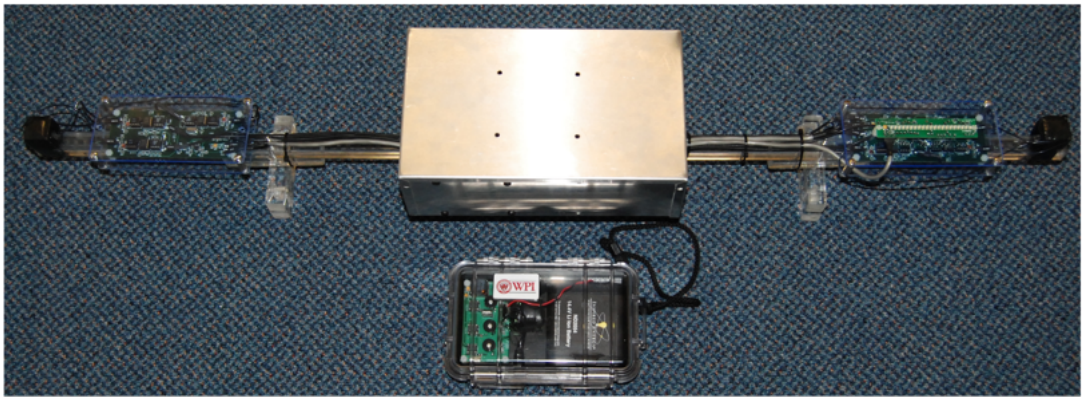

Figure 1.4: Mantenna Version 4 Receiver Wand and Transmitter

With the Mantenna system, every firefighter would enter a scene with a Mantenna transmitter (antenna and associated electronics). Similar to the PPL system's transmitter, the Mantenna transmitter must be integrated into the firefighter's PASS device, or closely coupled to it. As a firefighter performs his/her duties, the transmitter will not transmit a signal. If the firefighter should become in distress, such as low on air, not moving for a fixed period of time, or depressing the panic button, the PASS device will activate and emit a loud audio tone. Upon activation of the PASS device, the Mantenna's transmitter will start transmitting the RF signal for the rescuer to locate.

The Mantenna's transmitter transmits the signal on all three axes, meaning the reception pattern is truly omnidirectional, as described in Section 3.2. This means the orientation of the distressed firefighter does not inhibit the search effort as the transmitter orientation shifts. This also means the rescuer can approach from any direction and receive the signal.

A second firefighter, acting as the rescuer, uses the Mantenna Receiver Wand to locate the distressed firefighter. The wand receives the RF signal from the transmitter and directs the rescuer to the distressed firefighter. By sweeping the wand from left to right and up and

down, the wand indicates the direction and distance to the distressed firefighter with an increasing tone, visual display, and vibration. The wand has an LED bar which increases the number of lit LEDs to indicate an approximate relative distance to the transmitter, and an audio tone and vibration which get correspondingly higher in frequency as the rescuer gets closer to the target or points in the correct direction.

During the search for the distressed firefighter, the rescuer sweeps the wand from left to right and up and down to determine which general direction the strongest signal is coming from. The direction in which to proceed is the wand's direction in which the largest number of LEDs on the indicator bar graph are lit, the highest pitched audio tone is heard and/or the most vibration is felt. The wand essentially acts as a Geiger counter for locating distressed personnel.

The system achieves best performance by having a rescuer (or several rescuers) first perform a perimeter search of the building from outside. This exterior search allows the elimination of large portions of a building, roughly 100 foot diameter zones, and allows the rescuer to quickly converge on the distressed person's general location. Once a general target area/zone is identified, the rescuer can enter the building and very quickly converge upon the distressed firefighter.

The rescuer then traverses the interior of the building toward the area with the strongest signal, periodically performing the sweep and correcting the trajectory as necessary. The increasing tone and visual display will inform the rescuer that he/she is going in the correct direction.

Unlike the PPL system, the Mantenna system does not keep a record of the distressed firefighter's path, nor does it send the location data to a display for the Incident Commander. Thus, a rescuer is directed to the distressed firefighter by the wand, not by the Incident Commander, as seen in Fig. 1.5. This means the rescuer (or rescuers) is entirely responsible for using the receiver wand to locate the distressed firefighter, unlike the PPL system where the Incident Commander directs the rescuer to the distressed firefighter with the aid of a display and previous path history.

1.6 Near Field Locator

This thesis expands upon the Mantenna Project by also exploring the potential for location and tracking using the same Near Field concepts developed in the course of the

Figure 1.5: Mantenna Receiver Wand Directing Firefighters

Mantenna Project. The work comprises two major components:

1. Improved transmitter system design - during which improvements were made that benefit both the homing and location applications.

2. Proof of concept for a Near Field Location and Tracking Rescue System - during which it is shown that a Near Field Location system is feasible.

The relevant electromagnetic theory and motivation for using the near field is described in Chapter 2. Chapter 3 describes some of the basic operating principles in the Mantenna homing system as well as provides a brief description of the hardware.

The improved transmitter system design was undertaken to reduce the size of the transmitter, in order to make it less bulky and more practical to carry. The previous system's air core antenna was reduced in volume via a ferrite core while striving to maintain the same radiation resistance, so as not to sacrifice the system's performance when reducing the physical size. Chapter 4 describes this effort in detail.

In addition, the limitations encountered by the PPL Position and Tracking Rescue System warranted an investigation of a Near Field Location and Tracking Rescue System. The PPL system has been unable to overcome the effects of multipath in extremely harsh

RF environments. The literature and initial tests showed that materials which cause multipath for the radiation far field appear transparent to the Mantenna [8], prompting a more thorough investigation of a Near Field Location System. Chapter 5 describes this effort in detail.

A Near Field Location and Tracking Rescue System will be similar to the current PPL system, with radiation far field hardware/technology replaced by the Mantenna Near Field technology. A transmitter will be worn by every firefighter who arrives on a scene, and modified Mantenna receiver wands will be mounted on fire trucks which surround the scene.

Each transmitter signal occupies 3kHz of bandwidth, hence succesive 3kHz bands can support distinguishable transmitters. Since the bandwidth available in the 1600 meter band is 30kHz, 10 simulatenous transmitters can be accomodated with the current design. Since the transmitter carriers are unmodulated, future versions can accomodate more transmitters by more closely spacing the carriers. Each transmitter will transmit continuously, with the receiver wands continuously receiving the signal and sending data to the Incident Commander's vehicle. The Incident Commander's vehicle will perform the necessary signal processing and display the location of several firefighters in real-time on a screen. Similar to the PPL system, the Near Field Location System will allow the Incident Commander to view the location of every firefighter in real-time on a screen, view the path traversed by any firefighter, display vital signs of each firefighter, and allow a rescuer to be directed to a firefighter in distress. The advantage of the Mantenna Near Field system comes from the ability to obtain accurate position estimates in extremely harsh RF environments where the PPL system would fail. An overview of what such a system would look like is depicted in Fig. 1.6.

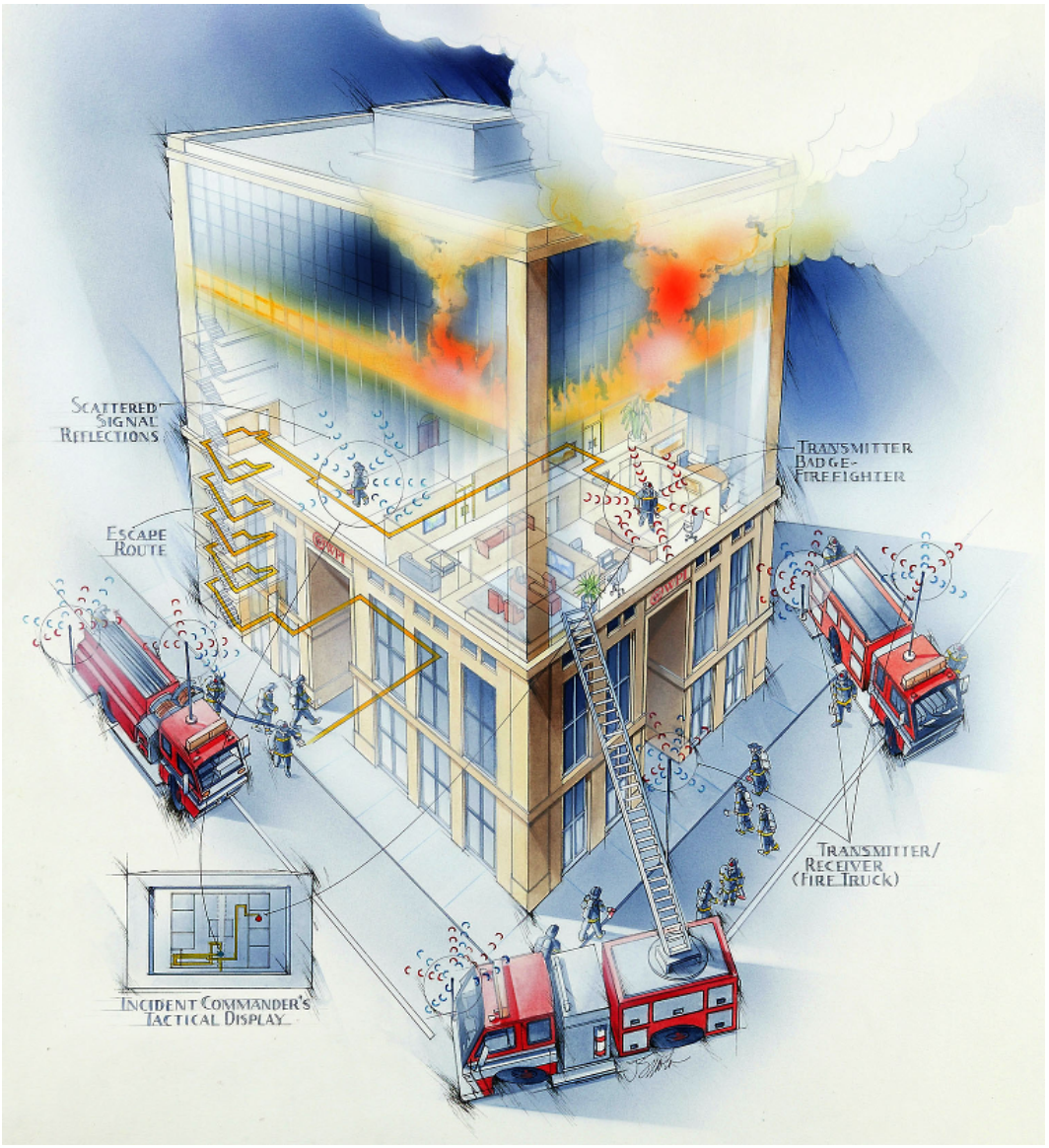

Figure 1.6: Location System Overview

Chapter 2

Near Field Theory

This chapter will introduce the necessary background knowledge to describe the Mantenna RF behavior. The near field is important with regard to building penetration, as metal surfaces, concrete, aluminum siding, pipes, etc. would block High Frequency (HF) and Far Field fields.

The basics of electromagnetic waves can be found in any undergraduate electromagnetics textbook, such as [9]. In addition, antenna basics, excluding ferrite loaded loop antennas, can be found in [10].

Using Maxwell's equations, one can derive the radiation pattern of a Hertzian dipole antenna, such as described in [9], as well as the radiation pattern of a magnetic loop antenna, such as described in [10].

2.1 Loop Antennas

The Mantenna uses a magnetic loop antenna. From [10], we see the fields emitted by a magnetic loop antenna placed at the origin and transmitting along the Z axis are given by Eq. 2.1.

$$\begin{aligned} H_r &= j\frac{ka^2 I_0 \cos(\theta)}{2r^2}\left[1+\frac{1}{jkr}\right]e^{-jkr} \\ H_\theta &= -\frac{(ka)^2 I_0 \sin(\theta)}{4r}\left[1+\frac{1}{jkr}-\frac{1}{(kr)^2}\right]e^{-jkr} \\ H_\phi &= 0 \\ E_r &= E_\theta = 0 \\ E_\phi &= \eta\frac{(ka)^2 I_0 \sin(\theta)}{4r}\left[1+\frac{1}{jkr}\right]e^{-jkr} \end{aligned} \tag{2.1}$$

where η = intrinsic impedance, I_0 is the current distribution in the wire, a is the radius of the loop, and k is the wavenumber where $k = \frac{\omega}{c} = \frac{2\pi}{\lambda}$. Eq. 2.1 entirely describes the fields emitted by a loop antenna.

There are three separate magnetic fields emitted by the magnetic dipole. The first is the Coulomb field, which falls off as $\frac{1}{r^3}$. The second is the Induction field, which falls off as $\frac{1}{r^2}$. The third field is the Radiation field and this field falls off as $\frac{1}{r}$. The Coulomb and Induction fields are referred to as the Near Field while the Radiation Field is normally referred to as the far field. The near field is advantageous to the Mantenna due to its shield penetration properties described in Section 2.2.

Often, the equations in Eq. 2.1 are approximated when working in the near field, as detailed in Section 2.1.1, or in the far field, as seen in Section 2.1.2.

2.1.1 Near Field Region

The expression for the radiated fields, given by Eq. 2.1, can be simplified when in the near field, $kr << 1$. The dominating term for the field in the near-zone region is the Coulomb portion of Eq. 2.1. Thus for $kr << 1$, Eq. 2.1 reduces to:

$$\begin{aligned} H_r &\simeq \frac{a^2 I_0 e^{-jkr}}{2r^3}\cos(\theta) \\ H_\theta &\simeq \frac{a^2 I_o e^{-jkr}}{4r^3}\sin\theta \\ H_\phi &= E_r = E_\theta = 0 \\ E_\phi &\simeq -j\eta\frac{a^2 k I_0 e^{-jkr}}{4r^2}\sin(\theta) \end{aligned} \tag{2.2}$$

The condition of $kr << 1$ can be satisfied at small distances away from the antenna, such as a distance $d < \frac{\lambda}{2\pi}$[10].

2.1.2 Far Field Region

Most radio applications use the long range properties of the far field, $kr >> 1$. Unlike the near field, the dominant term from Eq. 2.1 with $kr >> 1$ is the radiation term. For $kr >> 1$, the H_r component will be small compared with H_θ, and can be assumed to be

approximately zero. Thus, for $kr >> 1$, Eq. 2.1 reduces to:

$$H_\theta \simeq -\frac{k^2 a^2 I_0 e^{-jkr}}{4r} \sin(\theta) \tag{2.3}$$
$$E_\phi \simeq \eta \frac{k^2 a^2 I_0 e^{-jkr}}{4r} \sin(\theta)$$
$$H_r \simeq H_\phi = E_r = E_\theta = 0$$

The **E** and **H** field components of the loop antenna in the far field ($kr >> 1$) region are perpendicular to each other and transverse in the direction of propagation. They form a transverse electromagnetic (TEM) field whose wave impedance is equal to the intrinsic impedance of the medium [10]. A transverse wave is reflected by an ideal metallic sheet, leading to the direct path signal attenuation and multipath experienced by a far field system such as the PPL system discussed earlier. On the other hand, near field signals have significant shield penetration properties which the Mantenna takes advantage of, as described in Section 2.2.

2.2 Near Field Penetration

To be useful, the near field zone has to be large enough to represent distances of interest in a search. To satisfy the near field distance of $d < \frac{\lambda}{2\pi}$ described in Section 2.1.1, the wavelength must be large enough such that d falls within the desired distance. Thus a wavelength of several hundred meters or more must be chosen, and consequently a low frequency must be used. In the United States the only license free band that supports such experimentation is the 1600 meter band.

The near field will penetrate a metal shield with less attenuation than the far field as described in [8]. As seen in [11], the magnetic component of the field will penetrate a metal shield with less attenuation than the electric component, thus making the magnetic field more advantageous for the Mantenna.

A plot of effective shielding caused by a shield separating two magnetic dipoles as a function of frequency is presented in Fig. 2.1. The shielding equation presented in Eq. 34 from [12] describes only the attenuation caused by the shield and does not include attenuation of free space propagation. The parameters were selected such that Fig. 2.1 presents the effective shielding caused by a typical example of aluminum siding (thickness of 0.019 inches) as would be found on a residential structure for two magnetic dipoles

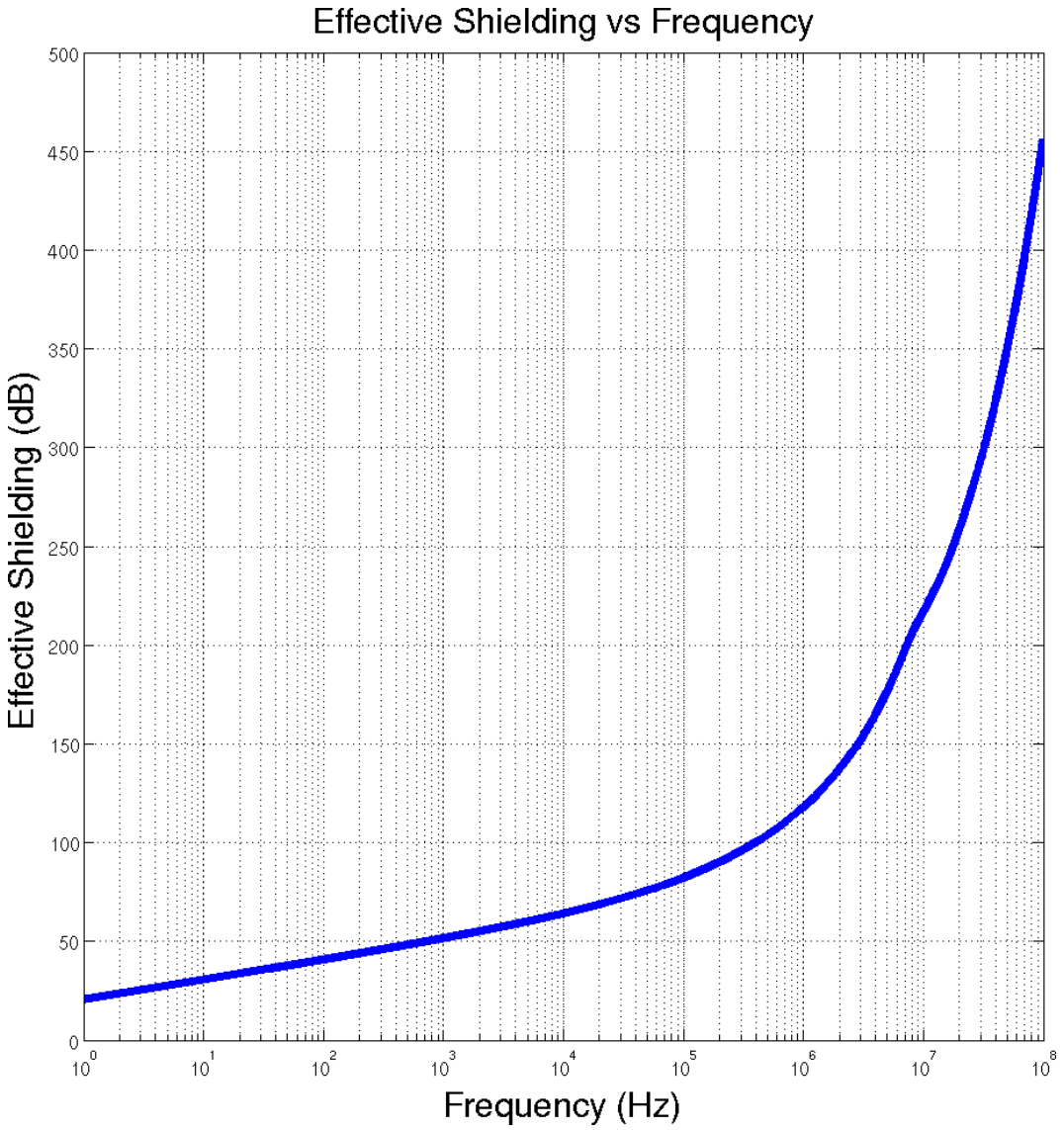

Figure 2.1: Effective Shielding of Aluminum Siding vs Frequency

placed 10 meters apart (each dipole being 5 meters from the shield) and facing each other as a function of frequency.

Fig. 2.1 shows the attenuation caused by aluminum siding for the Mantenna's VLF band is approximately 88dB (for $f = 170kHz$), and the attenuation caused by the same siding for the VHF band is approximately 456dB (for $f = 100MHz$). Recall that the radiation field falls off as $\frac{1}{r}$, corresponding to a loss of 6dB per octave (6dB attenuation for every doubling of free space propagation distance); the Coulomb field falls off as $\frac{1}{r^3}$ for a loss of 18dB per octave.

For the Near Field in the VLF band, the attenuation of 88dB by the aluminum siding

corresponds to $\frac{88dB}{18dB} \approx 4.9$, which acts as an apparent distance increase of $2^{4.9} \approx 30$ times. For the VLF radiation far field, the attenuation of 88dB caused by the shielding corresponds to $\frac{88dB}{6dB} \approx 14.7$, which acts as a distance increase of $2^{14.7} \approx 26,616$ times. For the radiation far field in the UHF band, the attenuation of 456dB by the siding corresponds to $\frac{456dB}{6dB} = 76$, which corresponds to a distance increase of $2^{76} = 7.5558\text{x}10^{22}$ times in distance. Thus the least attenuation induced by a shield is for low frequency near field signals.

Thus, the analysis of Fig. 2.1 using the shielding equation from [12], along with the information provided in [8] and [11] clearly present the importance of the magnetic near field for the Mantenna. The magnetic near field in the VLF band has significant shield penetration properties which allow most building structures to appear transparent to the Mantenna, thus dictating its use in order to attain good performance in high multipath environments.

Chapter 3

Mantenna and Near Field Locator Operating Principles

This chapter will describe the basic operating principles of the Mantenna and the Near Field Locator. Detailed is why the Mantenna is implemented the way it is as well as some of the decisions which were made in order to achieve a practical Homing System.

Fundamental to the Mantenna concept is a transmitter which is embedded in the gear of firefighters (or other emergency responders) such that when a person is in distress, it is activated. The receiver wand then senses the signal and guides the rescuer to the distressed person. The wand uses the signal strength to estimate the distance to the person in distress. This distance estimate is indicated as an audio tone of increasing pitch as the wand is brought closer to the target, and also as an LED display which is progressively lit.

For the Mantenna Homing system to work in modern buildings, such as commercial, industrial and apartment buildings, it must be able to perform well in harsh RF environments. Modern buildings are akin to a Faraday Cage with all the reinforced concrete, metal duct work, metal studs, coated energy efficient glass, fire doors and other metallic objects installed during construction. To achieve penetration in such environments the Mantenna uses the near field properties of low frequency electromagnetic waves as the near field has significant shield penetration properties as detailed in Chapter 2. While the near field only extends for a fraction of the wavelength, such as $\frac{\lambda}{2\pi}$, the use of a low frequency near $f \approx 170kHz$ means the wavelength is $\lambda \approx 1700$ meters and thus the near field can span for several hundred meters.

3.1 Wand Directionality

The receiver wand must be able to point the rescuer in the direction of the distressed firefighter, and it must not be ambiguous by leading one in the wrong direction (i.e. 180° from the transmitter). Leading the rescuer in the wrong direction, for whatever reason, is not acceptable as it will increase the amount of time necessary to rescue distressed personnel. In emergencies, time is critical, and any event in which the rescuer is not directly lead to the target will waste valuable time and potentially hinder rescue efforts.

The ability to point the rescuer to the source is inherent to the way the ordinary magnetic dipole antenna works due to its near field iso-surface, as described with the aid of Fig. 3.1. Fig. 3.1(a) depicts a magnetic dipole at the origin transmitting along the +Z-axis and a receiving magnetic dipole placed along the +Z-axis. Fig. 3.1(b) depicts the corresponding iso-surface for the transmitting antenna as seen by the receiving antenna. From Fig. 3.1(b) it is clear that the receiving antenna sees the strongest signal when the transmitting antenna is oriented along the +Z-axis; as the angle of the transmitting antenna is changed along the X-axis or Y-axis we see a reduction in the amplitude of the signal received, until no signal is received when the transmitting antenna is pointed orthogonal to the Z-axis. However, as the transmitter's angle is further changed, the amplitude of the signal received again increases, until it is again the maximum when pointing along the negative Z-axis.

Examining the iso-surface seen in Fig. 3.1(b), we see this leads to an interesting problem as the receiving antenna senses the same signal amplitude when the source is pointed directly at the receiving antenna and when the source is facing directly away from the receiving antenna.

A fix for the ambiguous direction problem is found by using a pair of antennas on the receiver wand, one mounted at the front and the other mounted at the rear. When the front antenna has a higher amplitude than the rear antenna, it is assumed the front of the wand is pointed toward the source. The "indicator value" (audio tone and displayed indicator) is a function of the front and rear receiver amplitudes such that it is a maximum when pointing directly at the transmitter and dropping to zero when pointing directly away from it.

Fig. 3.2 depicts a Mantenna wand pointed at the transmitter. The transmitter's iso-amplitude field pattern is depicted by the circle surrounding the transmitter and is uniform,

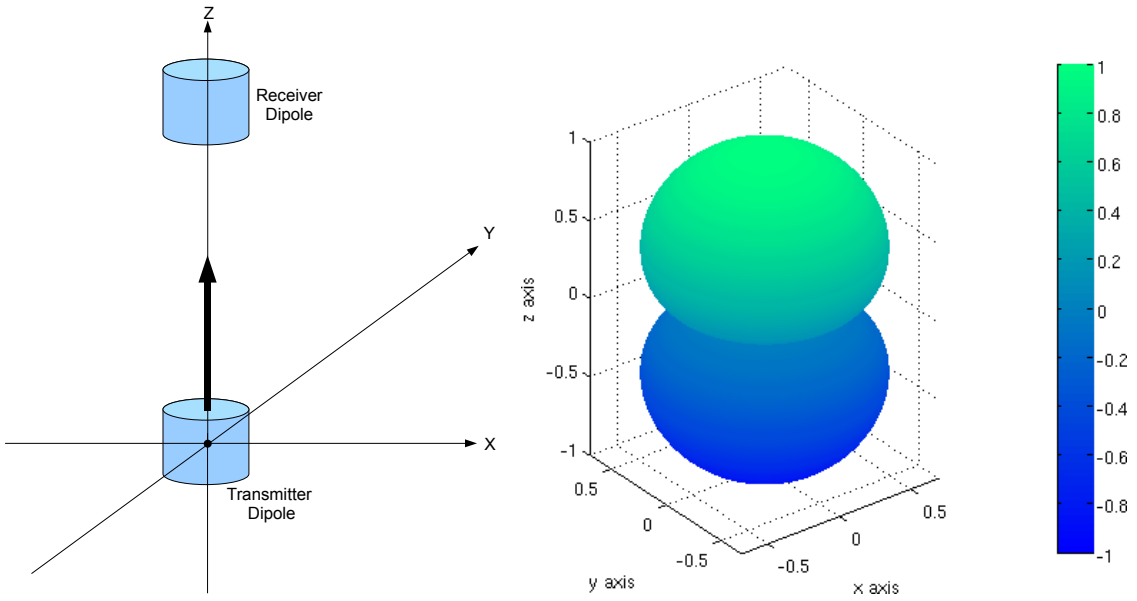

(a) Loop Orientations (b) Iso-surface

Figure 3.1: Three Dimensional Magnetic Dipole Relative Coulombic field amplitude iso-surface for a magnetic loop at the origin with axis aligned with Z coordinate axis

as described in Section 3.2. The receiver wand has a pair of antennas which sense the transmitter signal with the directivity as depicted by the circles surrounding each antenna.

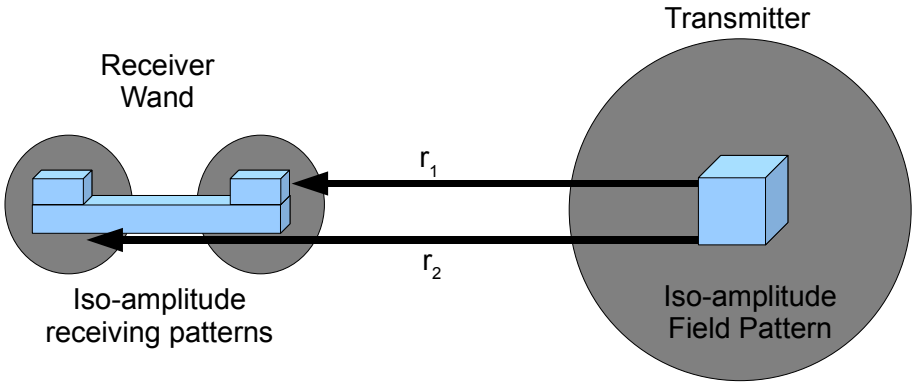

Figure 3.2: Mantenna Operation - Orientation 1

The distance between the wand's front antenna and the transmitter is depicted by r_1, and the distance between the wand's rear antenna and the transmitter is depicted by r_2. The Coulomb field falls off as a function of $\frac{1}{r^3}$, thus the difference in signal magnitude received by both wand antennas is defined as per Eq. 3.1.

$$D = \left(\frac{1}{r_1^3} - \frac{1}{r_2^3} \right) \tag{3.1}$$

From Eq. 3.1 we see the difference of received signal amplitudes at the receiver is a monotonic function of distance when the receiver wand is pointed directly at the source.

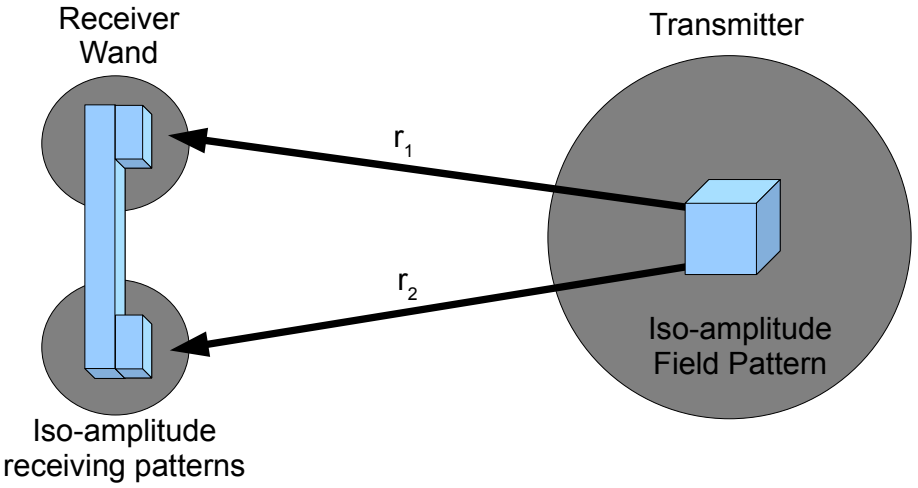

Figure 3.3: Mantenna Operation - Orientation 2

In Fig. 3.3, the wand is oriented such that the distance between the receiver wand's antennas in relation to the transmitter is equal, or $r_1 = r_2$. The difference of signal magnitude received by both wands in this case is therefore $D = 0$. This shows the difference is highly dependent upon the angle of the receiver wand relative to the source. Thus the Mantenna provides unambiguous information about the direction to the target as well as the notion of distance from it as described by Eq. 3.1.

In addition to the use of magnetic loop antennas on the receiver wand, the transmitter uses magnetic loop antennas. The use of a single magnetic dipole on the transmitter system would lead to a problem wherein the rescuer's signal would be entirely dependent on the orientation of the person in distress. To overcome this problem, three orthogonally placed magnetic dipoles are used, as described in Section 3.2.

3.2 Omnidirectional, Tri-Frequency Transmitter

This section describes the importance of the omni-directional transmitter antenna's field pattern and the motivation for the tri-frequency transmitter system. This omni-directionality allows the firefighter to be oriented in any way while still allowing the rescuer to approach from any angle as opposed to what arises for dipole antenna patterns if both transmitter and receiver were to use a typical single magnetic loop element, as described in Section 3.1.

To start, we observe the magnetic portion of the Eq. 2.1. Paying attention to the Coulombic Field, the portion which is a function of $\frac{1}{r^3}$ since we're observing the transmitter at distances where the Coulomb term dominates, we see the field scales as:

$$\frac{\cos^2(\theta)}{r^3} \tag{3.2}$$

If we set this equal to a constant, such as 1, we can then solve for where the field amplitude is unity for a given distance. Solving for r one gets:

$$r = \sqrt[3]{\cos^2(\theta)} \tag{3.3}$$

Eq. 3.3 describes the amplitude pattern of the magnetic dipole and gives the distance from the origin at which the amplitude is constant for the given angle θ. For a single magnetic dipole, this field pattern can be plotted in 3D as per Fig. 3.1(b).

To achieve the omnidirectional field pattern desired on the Mantenna, we can place three magnetic dipoles orthogonal to each other. Ordinarily we cannot simply sum the amplitudes of three antennas without taking into account the effects of phase related cancellation. However, for reasons to be explained below, we will assume for the moment that a purely additive approach can be used.

Now, one can recast the field given in Eq. 3.2 for the case of three non-interfering, that is, additive, fields as per Eq. 3.4.

$$\frac{\cos^2(\theta_x)}{r^3} + \frac{\cos^2(\theta_y(\theta_x, \phi_x))}{r^3} + \frac{\cos^2(\theta_z(\theta_x, \phi_x))}{r^3} \tag{3.4}$$

As with the single axis case, we will set the quantity in Eq. 3.4 equal to a constant. Then we can solve for the distance r in three space where the total amplitude is constant and generate the new three dimensional amplitude pattern.

Using simply trigonometric identities, we observe that we can find the value of θ_x along the x-axis by taking the arc-cosine of the amplitude x_p along the x-axis; similarly, we can find the value of θ_y along the y-axis by taking the arc-cosine of the amplitude y_p along the y-axis, and also the value of θ_z by taking the arc-cosine of the amplitude z_p along the z-axis. Then, we can substitute $\theta_x = \arccos(x_p)$, $\theta_y = \arccos(y_p)$, and $\theta_z = \arccos(z_p)$

into Eq. 3.4 to yield:

$$\begin{aligned}
\frac{\cos^2(\theta_x)}{r^3} + \frac{\cos^2(\theta_y(\theta_x,\phi_x))}{r^3} + \frac{\cos^2(\theta_z(\theta_x,\phi_x))}{r^3} &= 1 \\
\frac{\cos^2(\arccos(x_p))}{r^3} + \frac{\cos^2(\arccos(y_p))}{r^3} + \frac{\cos^2(\arccos(z_p))}{r^3} &= \\
\frac{(\cos(\arccos(x_p)))^2}{r^3} + \frac{(\cos(\arccos(y_p)))^2}{r^3} + \frac{(\cos(\arccos(z_p)))^2}{r^3} &= \\
\frac{x_p^2}{r^3} + \frac{y_p^2}{r^3} + \frac{z_p^2}{r^3} &= 1 \qquad (3.5)
\end{aligned}$$

We see that Eq. 3.4 reduces to the equation of a sphere in three space. This shows the amplitude pattern in three dimensions of the three orthogonally placed magnetic loop antennas for an additive near field is perfectly uniform; no matter from which angle the rescuer approaches the person in distress, they will receive the same signal amplitude and be able to locate the target. Fig. 3.4 depicts the three orthogonally placed magnetic dipoles as specified by Eq. 3.5, where Fig. 3.4(a) depicts the placement of the loop antennas and Fig. 3.4(b) depicts the corresponding iso-surface seen at the receiver antenna placed along the +Z-axis.

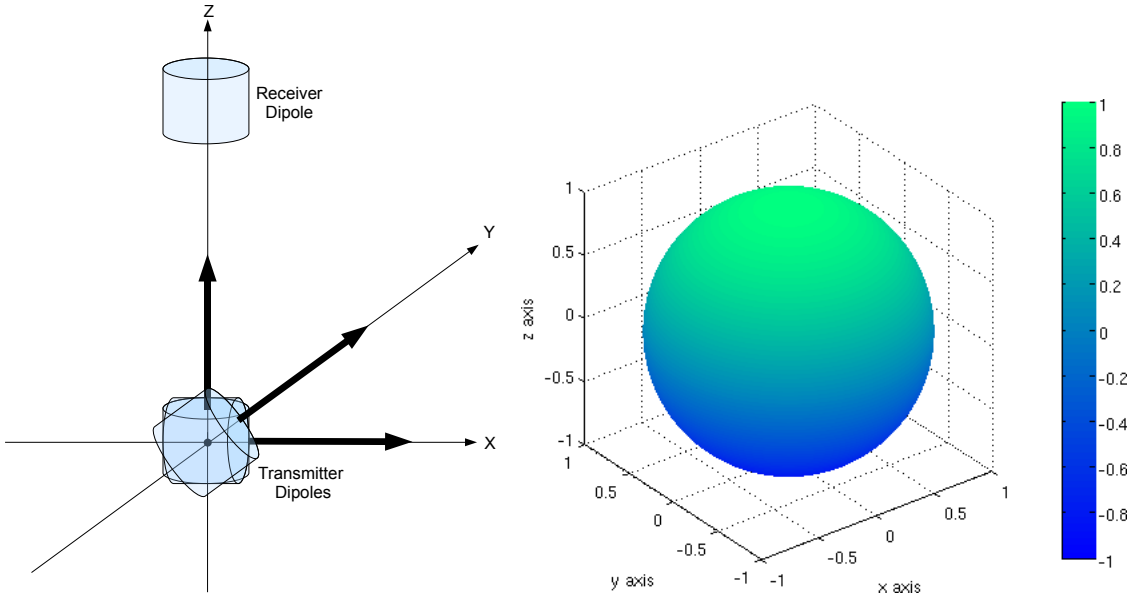

(a) Loop Orientations (b) Iso-surface

Figure 3.4: Three Dimensional Tri-Axial Additive Magnetic Dipole Amplitude Pattern

The three dipoles placed orthogonally on the transmitter system as per Fig. 3.4 is referred to as a tri-axial transmitter system. The significance of this tri-axial transmitter design is that it allows for a nearly orientation independent amplitude estimate of the

signal at the receiver, from which the distance can computed, solving the orientation independent homing problem. In addition, using the field amplitude sensed by multiple receivers surrounding a building, this allows for triangulation of the transmitter.

To achieve an additive amplitude behavior the same frequency signal is not transmitted by each of the three orthogonally placed antennas. Basic trigonometry reminds us that the sum of cosines of the same frequency can constructively add or destructively add, depending on the distance of the antennas and the phases at location of interest. This idea is used in beamforming and phased array radars, and more details can be found in any radar or antenna book, such as [10]. To avoid any cancellation, and to keep the receiver wand's signal independent of the transmitter orientation, it is necessary to use three separate carrier frequencies, one for each antenna. At the receiver, the envelopes of the three carrier frequencies are found and simply added to obtain the desired behavior described by Eq. 3.4.

3.3 Mantenna System Hardware

The next sections discuss the Mantenna Homing System hardware. The basic principles of how the hardware works will be discussed and will include block diagrams as appropriate to help with the explanation. Recall that the Mantenna System consists of two components, as seen in Fig. 1.1, a transmitter worn by the firefighter as seen in Fig. 1.1(b) and the receiver wand used by the rescuer as seen in Fig. 1.1(a).

3.3.1 RF Front End Hardware

The author was not involved in the design and implementation of the receiver's RF Front End board (RFFE) but will briefly summarize its operation here. The Receiver Wand contains a pair of RFFE boards. These boards take the signal from the antennas, all three axes, and performs the necessary frequency conversions to baseband before feeding the analog signal to the DSP. The DSP operations are described in Section 3.3.2. Fig. 3.5 shows a block diagram of the RFFE.

Each antenna has its own RF Amplifier and Mixer/Oscillator pair. The transmitter transmits on three frequencies spaced 1kHz apart, as given in Table 3.1. The receiver antennas sense all three frequency components, and the mixer/oscillator stages of the antennas are tuned such that the result of the frequency conversion yields signals with

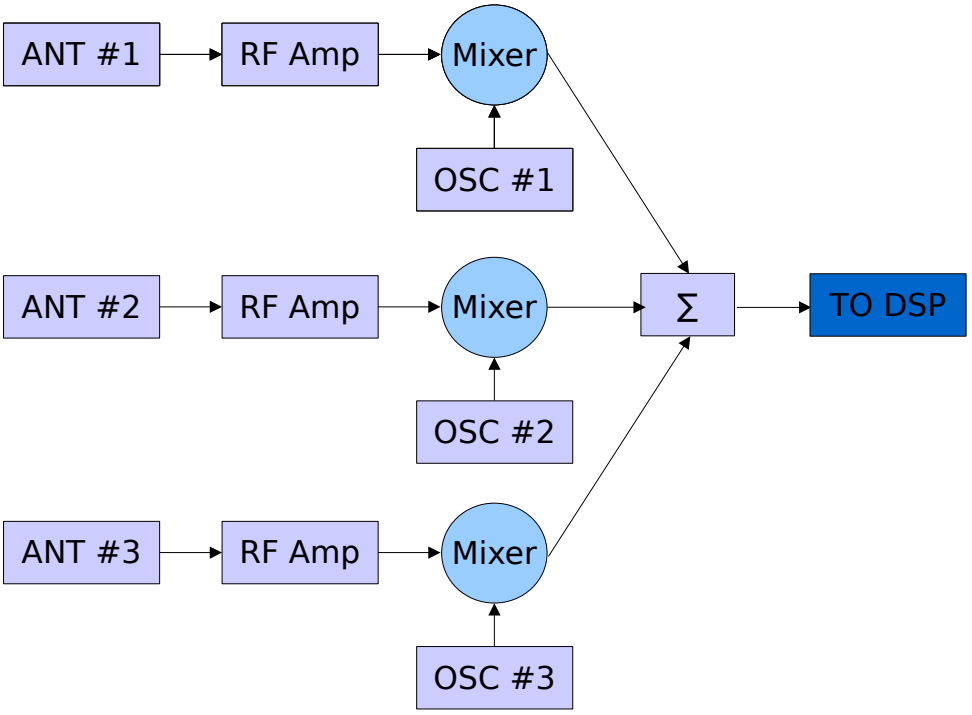

Figure 3.5: RF Front End Block Diagram

frequencies of 1kHz, 2kHz, 3kHz, 4kHz, 5kHz, 6kHz, 7kHz, 8kHz, and 9kHz. For clarity, Table 3.1 summarizes which frequencies are associated with which antenna orientations for the Transmitter frequencies. The frequency of the oscillator determines the baseband frequencies into which the transmit frequencies are converted by the mixer stage. The signal is mixed down to allow the use of the DSK's Analog-to-Digital (A/D) converter. The A/D can sample audio frequencies (up to 20kHz), meaning we can take advantage of this already available A/D by performing the frequency conversions.

For example, the transmit frequency of $f_1 = 170kHz$ is sensed by all three antennas, and the result of frequency conversion by the first mixer/oscillator stage is a signal at $f = 1kHz$, the second antenna's frequency conversion stage yields a signal at $f = 4kHz$, and the third antenna's frequency conversion stage yields a signal at $f = 7kHz$. The output of all three mixer/oscillator stages is summed via an op-amp, then sent to the DSK for processing.

Table 3.1: Frequency and Orientation Reference

Trans. Freq.	Mixer Freq.	Mixer Output	Rec. Ant.	Rec. Ant. Orientation
170kHz	169kHz	1kHz	1	Front/Back
171kHz	169kHz	2kHz	1	Front/Back
172kHz	169kHz	3kHz	1	Front/Back
170kHz	166kHz	4kHz	2	Left/Right
171kHz	166kHz	5kHz	2	Left/Right
172kHz	166kHz	6kHz	2	Left/Right
170kHz	163kHz	7kHz	3	Up/Down
171kHz	163kHz	8kHz	3	Up/Down
172kHz	163kHz	9kHz	3	Up/Down

3.3.2 Digital Signal Processing

The Mantenna makes use of a DSP Starter Kit (DSK) based upon the Texas Instruments TMS320C6713 Floating Point Digital Signal Processor. This low cost DSK is made by Spectrum Digital and contains the C6713 DSP, an audio codec (we use as an A/D and D/A), peripheral ports, compiler and necessary software.

The Mantenna DSP software implements a series of novel signal processing algorithms specific for the Mantenna's needs. The author was not involved with the majority of the development of these algorithms, but has maintained and improved the algorithms as needed. A block diagram of the DSP algorithms is seen in Fig. 3.6.

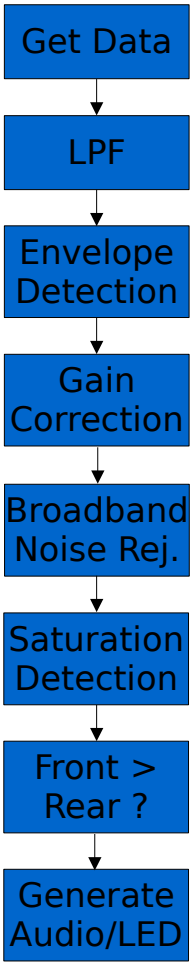

Figure 3.6: Mantenna DSP Block Diagram

The algorithms start by obtaining a sample from the DSK's audio codec. Low pass filtering then occurs to break the input signal into the nine frequency components originally observed at the RF Front End board. The envelope detection algorithm converts the

sinusoidal/high frequency input signal for each of the nine frequencies into an envelope (constant amplitude).

The gain correction stage applies the calibration values to scale the amplitudes in order to give each component equal weighting - this corrects for small differences in the antenna and RF front end implementations.

Next, the broadband noise rejection stage rejects any interference caused by a broadband power source, such as fluorescent lights, power conduits, etc. If broadband noise is detected, the output is scaled down to prevent a false indication of proximity to the true transmitter; as the noise disappears, the output is scaled back to the normal value.

Next, the front and rear antenna amplitudes are checked to determine whether the wand is in saturation mode. If it is, the LED bar graph and audio tone will be pulsed in addition to their normal behavior.

The above steps occur in parallel for the data from the front of the Mantenna receiver wand and the rear of the Mantenna receiver wand. The data from the front and rear are used simultaneously for the final processing stages.

The second to last step involves comparing the front and rear antenna values to determine which way the wand is pointed. If the front antenna has a stronger signal, the front of the wand is pointed at the transmitter and the audio tone and LED bar graph are generated. If the rear antenna has a stronger signal, the audio tone and LED bar graph are shut off. The generated audio tone and LED bar graph values are then given to the D/A which is connected to the LED bar graph circuitry and audio tone circuitry.

3.3.3 Transmitter

The transmitter used consists of a simple design. A block diagram is seen in Fig. 3.2.

The transmitter consists of three separate oscillators, power amplifiers, and antennas to produce the necessary signal. Each stage is identical, except for the frequency generated. Each oscillator is tuned to a different carrier frequency to satisfy the conditions described in Section 3.2. The carrier is then amplified with a power amplifer, consisting of a BJT push-pull amplifier. This amplified signal is then transmitted by the antenna.

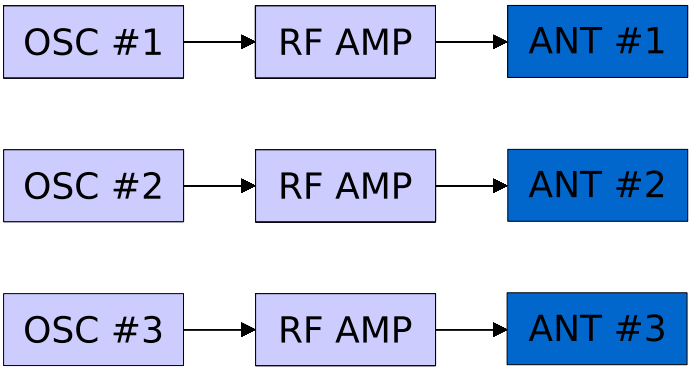

Figure 3.7: Transmitter Block Diagram

Chapter 4

Transmitter System Redesign

This section describes the transmitter system redesign, including the new antenna design, for the Mantenna Transmitter. The previous transmitter system design is briefly described to provide the motivation for the system redesign. The necessary background will be described, and the resulting new system design, including the new antenna design, will be summarized.

The old transmitter design is a large, proof of concept prototype which served during the development of the Mantenna system. The uniform field pattern required by the Mantenna is achieved by the use of a cube antenna for the transmitter, with "three" separate loop antennas sharing a single air core, one antenna for each axis (x, y, and z axes), as described in Section 3.2. Fig. 4.1 shows that the previous system design is rather bulky and unsuitable for use by emergency personnel as each side of the antenna cube is approximately $64.4mm$ in width; a smaller antenna is necessary if emergency personnel are expected to use the device.

It was decided that transmitter system redesign and reimplementation would be undertaken in order to make a more practical transmitter. The FCC power limits mean a high efficiency antenna is desired, however the goal of making a wearable transmitter means the antenna must be small yet efficient. The goal of the system redesign was to reduce the antenna size while maintaining the system's performance, in other words, the size reduction could not come due to a reduction in performance. The air core antenna can be replaced by a ferrite core, allowing for some reduction in size while maintaining the same field strengths. Through-hole electronics can be replaced by surface mount components, allowing for the circuit boards to be reduced in size.

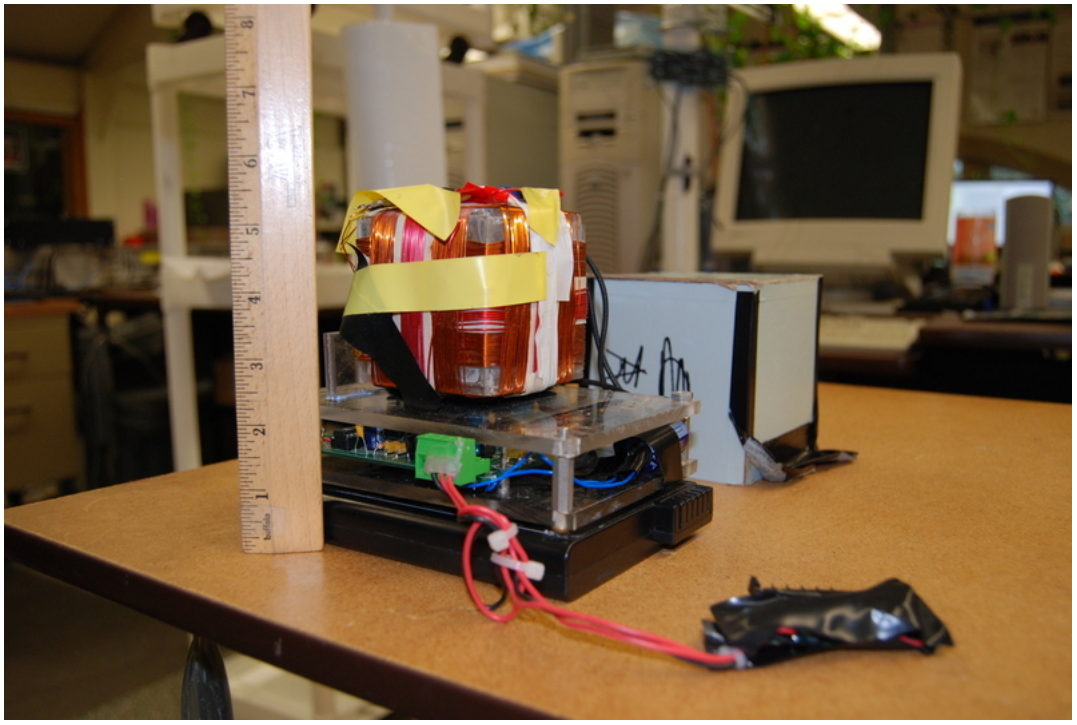

Figure 4.1: Previous Transmitter Design

4.1 Design Criteria for Transmitter New System

In determining a new system design, the following design criteria were decided to be critical: The antenna must be electrically small and physically small in order to be wearable by the firefighter. The antenna efficiency of the new system must be equal to or greater than that of the previous system, as the performance must not be sacrificed in order to achieve a size reduction. A bandwidth of $BW \geq 4kHz$ is required, as any less would render the antenna unusable owing to the use of 3 transmitted carriers that span the bandwidth. While each transmitter antenna is driven at a single frequency and hence may be allowed a narrower bandwidth, it was decided by my advisor that only one design be undertaken that would serve to replace the transmitter antenna and both receiver antennas. The latter must provide the full 4kHz bandwidth.

The antenna size can be reduced by replacing the air core with a ferrite core. The ferrite allows for a higher radiation resistance R_r for a given geometry. Conversely, theory predicts that a reduction to $\frac{1}{9}$ volume can be achieved using the ferrite while keeping the same R_r.

The move from a prototype system to a more deployable system renders through-

hole electronic components, various debugging points, and other development portions unnecessary. Removing the unnecessary parts and replacing through-hole components with surface mount components allows for a smaller printed circuit board. The smaller circuit board means a smaller overall footprint of the electronic components, and is a step towards a more deployable design.

Lastly, the design and test procedures must be fully documented. The above design criteria must be met, otherwise the new system will not be able to perform as well as the old system.

4.2 Antenna Theory and Models

This next section describes some of the antenna theory, specific to ferrite loaded loop antennas, needed to explain how and why certain parameters were selected as they are. In addition, two antenna models will be described which were the basis for the performance analysis and optimization that was conducted.

In the following we will choose antenna parameters so as to maximize antenna radiation efficiency (the ratio of radiated power to absorbed power) within other constraints. It might seem at first to be odd to be maximizing the radiation efficiency when in fact this is a near field system which depends in effect not at all on radiated signal power, but only the non-radiated near field intensity. There is however a strong link between the size of the radiated field and the size of the near field. As can be seen by looking at the full dipole antenna field equations, Eq. 2.1, for a dipole the near and far field components are directly proportional to each other. Hence, optimization of the efficiency and hence far field radiation for a given input power is tantamount to maximization of the near field amplitude for the same antenna.

4.2.1 Radiation Power Factor

The radiation power factor was introduced by H. Wheeler in his 1959 paper "The Radiansphere Around a Small Antenna" [13]. The radiation power factor describes how a change in antenna core permeability affects the radiation resistance of an antenna.

Wheeler gives the radiation power factor as Eq. 20 from [13]:

$$p = \frac{R}{\omega L} = \left(\frac{2\pi a}{\lambda}\right)^3 \cdot \frac{1}{1 + \frac{2}{\kappa_m}} \tag{4.1}$$

where R is the radiation resistance, ωL is the inductive reactance, κ_m is the permeability of the core and a is the radius of the sphere tightly enclosing the antenna.

As the bandwidth requirement is fixed by the signal structure being used, the minimum Q of the antenna, where Q is the ratio of the reactance of the inductance at resonant frequency to the resistance ($Q = \frac{2\pi f_0 L}{R}$), is also fixed (the relationship between bandwidth and Q will be discussed later). Given a fixed antenna Q and all other parameters fixed, the radiation power factor tells us there's a limit of a factor of 3 improvement in efficiency η which can be achieved by increasing the core permeability to infinity $\kappa_m \to \infty$ for a fixed antenna inductance.

Expressing the behavior captured by Wheeler's equation in terms of the desired Q of the antenna yields the equation for efficiency seen in Eq. 4.2.

$$\eta_{\kappa_m} = \frac{8Q\kappa_m\pi^3 a^3}{(\kappa_m + 2)\,\lambda^3} \tag{4.2}$$

Varying the value of κ_m from $0 \to \infty$ in 4.2, we see an increase in efficiency η_{κ_m} as κ_m increases, but this is not a linear relation as the increase in η_{κ_m} diminishes as κ_m gets larger. This nonlinear relationship is shown in Eq. 4.3, and plotted in Fig. 4.2.

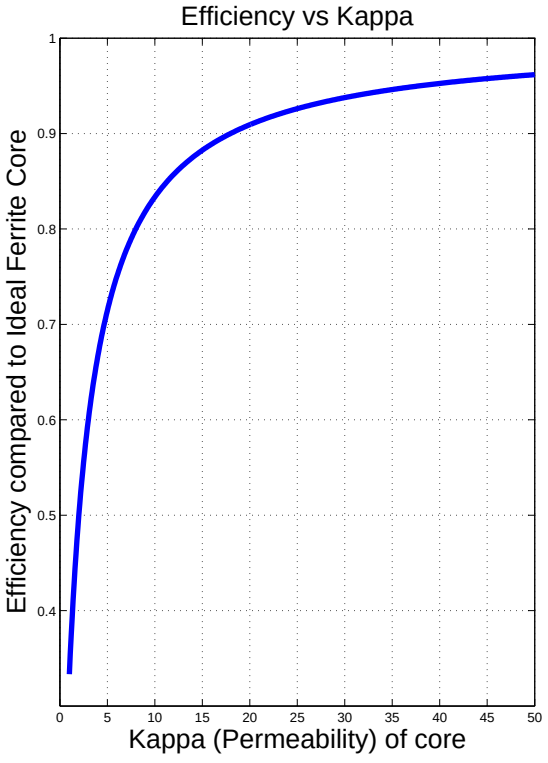

Figure 4.2: Efficiency vs Permeability

$$\begin{aligned}
\kappa_m = \ \ 1 \ &\Rightarrow \eta_{\kappa_m=1} \ \ = 0.3333 \cdot \eta_\infty \\
\kappa_m = \ \ 25 &\Rightarrow \eta_{\kappa_m=25} \ \ = 0.9278 \cdot \eta_\infty \\
\kappa_m = \ \ 50 &\Rightarrow \eta_{\kappa_m=50} \ \ = 0.9635 \cdot \eta_\infty \\
\kappa_m = 100 &\Rightarrow \eta_{\kappa_m=100} = 0.9824 \cdot \eta_\infty \\
\kappa_m = 500 &\Rightarrow \eta_{\kappa_m=500} = 0.9980 \cdot \eta_\infty
\end{aligned} \tag{4.3}$$

From Eq. 4.2 and Eq. 4.3, it's clear that there's a point at which an increase in the permeability κ_m does not translate to a substantial gain in the efficiency η. This allows for the selection of a ferrite core which has a "high enough" permeability κ_m that gives nearly all the increase seen by the ideal core $\kappa_m = \infty$. This is important as core losses play a factor in limiting the increase in radiation resistance R_r and hence efficiency η, as will be discussed in Section 4.2.2.

4.2.2 Loss Tangent

So, a ferrite core increases the radiation resistance of the antenna, but this increase does not come without an expense. The Loss Tangent of a ferrite dictates the ferrite resistance R_F, and the ferrite resistance determines how much power is dissipated by the core, as will be discussed in the next section.

There are three types of loss associated with ferrites, the hysteresis loss δ_h, the eddy current loss δ_e, and the residual loss δ_r. The Loss Tangent is usually written in the form of the Normalized Loss Tangent, as seen in Eq. 4.4, which is the combination of the three types of loss normalized by the permeability.

$$\frac{\tan(\delta)}{\kappa_m} = \frac{\tan(\delta_h)}{\kappa_m} + \frac{\tan(\delta_e)}{\kappa_m} + \frac{\tan(\delta_r)}{\kappa_m} \tag{4.4}$$

This loss tangent is important as the the ferrite resistance R_F is proportional to the loss tangent $\tan(\delta)$.

At sub-MHz frequencies, the hysteresis loss δ_h dominates [14]. The hysteresis loss occurs when a ferrite is placed in a magnetic field alternating about zero. After the initial magnetization occurs (during the first cycle), there is an induced magnetic field in the ferrite. Subsequent oscillations of the magnetic field about zero will cause a lag in the ferrite's induced magnetic field, and the initial magnetization curve will not be retraced. Thus, the induced magnetization lags behind the magnetic field and traces a loop, called

a magnetic hysteresis loop, as seen in Fig. 4.3. [14].

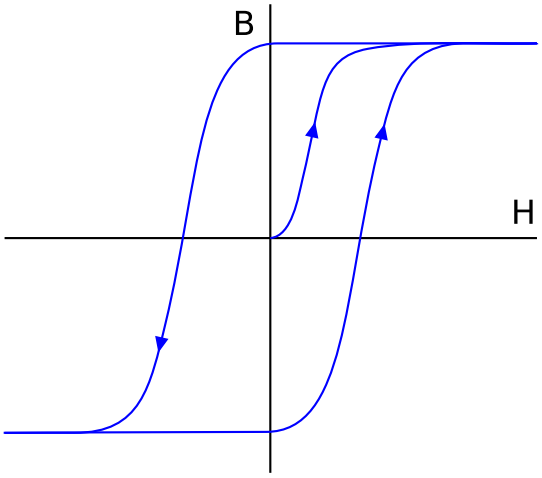

Figure 4.3: Hysteresis Curve

For more information on the chemistry of ferrites, how they're fabricated, a detailed explanation of the physics behind ferrites, and more information about the other types of losses, see the extremely informative text by Snelling [14].

Thus, the choice of a ferrite with a low Loss Tangent is desired, as it will reduce the power dissipated by the core, and hence increase antenna efficiency. This fact, combined with the fact that the permeability κ_m can be "high enough" as per Section 4.2.1, show that the priority for selecting a ferrite should be the lowest Loss Tangent and a "high enough" permeability.

4.2.3 Circuit Analog

The relationship between loop antenna efficiency, bandwidth, and core losses is best understood in terms of an equivalent circuit. The circuit analog of a loop antenna is depicted in Fig. 4.4:
where R_l = coil (conductor) loss, R_F = core loss resistance, R_r = radiation resistance, R_{in} = total loop resistance, C_{res} = resonant capacitor, L = loop inductance, f_0 = center frequency (Hz), and BW = 3dB bandwidth (Hz).

It is clear that:

$$R_{in} = R_l + R_r + R_F \tag{4.5}$$

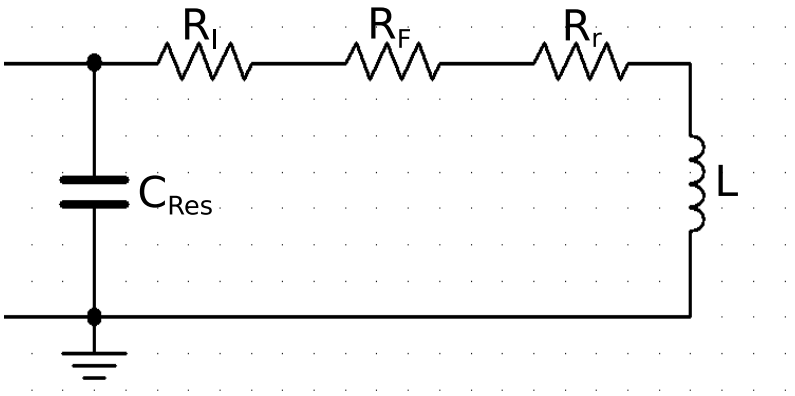

Figure 4.4: Circuit Analog of Loop Antenna

The bandwidth BW is defined as:

$$BW = \frac{f_0}{Q} = \frac{R_{in}}{\omega L} \cdot f_0 = \frac{R_{in}}{2\pi L} \tag{4.6}$$

The efficiency of the antenna, which is to be maximized, is given by η, and is defined as:

$$\eta = \frac{R_r}{R_{in}} \tag{4.7}$$

The efficiency describes the fraction of input power which is actually radiated by the antenna. The remainder of the power is lost either to the ferrite core, due to R_F, or to the wire due to R_l.

For the antenna redesign, two papers were used to implement two differing models for determining the new antenna's parameters. The first paper is from R. DeVore, [15] and the second is from Ted Simpson, [16]. These two models differ in the simplifications and approximations used. Despite the small differences between the models, the predicted outcomes differ substantially. Furthermore, as will be detailed below, the specifics of our antenna will differ from each model. Hence these models can only be used as guides for the design with final values experimentally determined. Thus both models were simulated to help best guide the final design. Additional background was provided by Professor Cyganski, [10] and [9].

The two models differ in the approximations and component geometry used in computing the parameters. For example, both models use an ellipsoidal core in their analysis in order to yield a closed form solution, while a cube will be used by the Near Field Locator's

(NFL) final design. Both models also assume the internal **B** field is uniform with only a **z** axis component; the NFL antenna has three antennas, one for each of the x, y, and z axes, which share a single core. Both models also use the Lorenz formula to approximate the coil inductance with a uniform current sheet, which results in a slightly different current distribution from the true current distribution which is bunched in each winding of the wire. Both models ignore any proximity effects which might occur with wire wound closely. The DeVore model assumes the use of circular wire while the Simpson model assumes the use of a Ribbon wire, giving slightly different skin effects. The Simpson model assumes the wire winding is of uniform spacing with the windings over the entire core.

A geometry is assumed in the DeVore paper comprising a thin ellipsoidal core of length l_F and radius a_F. This core is wrapped with a coil of radius $a \geq a_F$ for a length of l using a turn spacing of $2d$ and using a cylindrical wire of radius b. The Simpson paper assumes a geometry comprising an ellipsoidal core with the larger semi-principal axis having dimension a and the other dimension b. The entire ellipsoid is wound with a flat conductive tape of width p. See respective papers for figures.

The optimization problem for our case involves:

- Selecting materials / diameters - a_F (thickness of ferrite core), κ' (relative permeability of ferrite core), and κ'' (imaginary permeability of ferrite core)
- Assume a fixed l_F (length of ferrite core) and BW (bandwidth)
- Vary parameters N (number of wire turns), a (spacing between wire and ferrite core), l (length of wire windings on ferrite core), and b (thickness of wire) to maximize the efficiency η

MATLAB scripts were written to implement both models, to perform the variation of parameters, and to determine the optimal design.

4.2.4 Key Antenna Formulae

In the following section, equations for the antenna design will rely upon a large number of material, electrical, and geometric parameters. These variables have been collected below and are defined as:

- $\mu_0 = 4\pi 10^{-7} N/A^2$ - permeability of free space
- $\sigma = 59.6 \cdot 10^{-6} s/m$ - conductivity of copper

- $c = 299,792,458 m/s$ - speed of light
- $R_0 = 377\Omega$ - impedance of free space
- $\kappa' = \kappa_m = \mu_i = \mu$ - relative permeability of ferrite core
- κ'' - imaginary permeability of ferrite core
- $lossTangent = \delta$ - measure of how lossy the core is
- $f = Hz$ - center frequency, in Hz
- $\omega = 2\pi f$ - center frequency, in radians
- $\lambda = \frac{c}{f}$ - wavelength
- $a_{simp} = \left(\frac{3V_0 x^2}{4\pi}\right)^{1/3}$ - $\frac{1}{2}$ length of the core, aka $\frac{1}{2}$ length of the coil windings, aka semi-major axis
- $b_{simp} = \left(\frac{3V_0}{4\pi x}\right)^{1/3}$ - radius of the core (ellipse shape), aka semi-minor axis
- x - desired ratio of $\frac{a_{simp}}{b_{simp}}$
- V_0 - desired volume of the ferrite core
- $N = n$ - number of turns of wire (around core)
- $p = \frac{2 \cdot a_{simp}}{N}$ - wire width
- $a_{DeVore} = b_{simp}$ - DeVore radius definition
- $l = 2 \cdot a_{simp}$ - length of wire wrappings
- $b_{DeVore} = \frac{p}{2}$ - radius of the copper wire
- D = value of D given by Eqs. 4.23, 4.24, 4.25, and 4.26 with "l" = coil length l
- D_F = value of D_F given by Eqs. 4.23, 4.24, 4.25, and 4.26 with "l" = core length l_F

4.2.5 Simpson Equations

This section lists the equations used for simulation from the Simpson model. These are taken from the Simpson paper [16] and the correction to the Simpson paper [17].

Ellipsoid Parameter

If the antenna is treated as an ellipsoid, the curvature is given by ξ. This parameter is calculated from the length and radius of the antenna:

$$\xi = \frac{1}{\sqrt{1 - \left(\frac{b_{simp}}{a_{simp}}\right)^2}} \tag{4.8}$$

Area Encompassed by Coil

It is necessary to compute the total area encompassed by the several turns of the coil. This is calculated as follows in Eq. 4.9, taken from Eq. 21 in [16].

$$S_{coil} = \frac{2\pi N b_{simp}^2}{3} \tag{4.9}$$

F Parameter

The F parameter is used to help derive the magnetostatic field potentials for the antenna calculations. It is defined in Eq. 12 in [16].

$$F\left(\xi_0, \kappa_m\right) = \frac{\xi_0 \cdot Q1'(\xi_0)}{\xi_0 \cdot Q1'(\xi_0) - \kappa_m \cdot Q1(\xi_0)} \tag{4.10}$$

Antenna Inductance

The antenna inductance L is determined by Eq. 23 in [16].

$$L = \mu_0 \cdot \kappa_m \cdot \left(\frac{N}{2a_{simp}}\right) \cdot S_{coil} \cdot F\left(\xi_0, \kappa_m\right) \tag{4.11}$$

Core Loss Resistance

The core loss resistance R_F is determined by Eq. 6 in [17].

$$R_F = \omega \cdot \mu_0 \cdot \kappa'' \cdot \left(\frac{2 \cdot \pi \cdot N \cdot b_{simp}^2}{3}\right) \cdot \left(\frac{N}{2 \cdot a_{simp}}\right) \cdot \left|\frac{\xi_0 \cdot Q1'(\xi_0)}{\xi_0 \cdot Q1'(\xi_0) - \mu_r \cdot Q1(\xi_0)}\right|^2 \tag{4.12}$$

where μ_r is defined as:

$$\mu_r = \kappa' - j\kappa'' \tag{4.13}$$

and $|x|$ is the norm of x.

Radiation Resistance

The radiation resistance R_r is determined by Eq. 32 in [16].

$$R_r = \frac{R_0}{6\pi} \cdot \left(\frac{S_{coil}}{radianlength^2} \right)^2 \cdot \left[(1 + (\kappa_m - 1) \cdot F(\xi_0, \kappa_m))^2 \right] \tag{4.14}$$

where the *radianlength* is defined as:

$$radianlength = \frac{\lambda}{2\pi} \tag{4.15}$$

Conductor Resistance

The conductor resistance R_l is seen in Eqs. 4.16 and 4.17. This calculation depends on how the ellipsoid is shaped, whether it is prolate, Eq. 37 from [16], or oblate, Eq. 39 from [16].

For the prolate case, where $a_{simp} > b_{simp}$:

$$R_l = \frac{\pi}{2} \cdot R_s \cdot N^2 \cdot \sqrt{\xi_0^2 - 1} \cdot \left[\left(2 - \xi_0^2\right) \cdot \arcsin\left(\frac{1}{\xi_0}\right) + \sqrt{(\xi_0^2) - 1} \right] \tag{4.16}$$

For the oblate case, where $a_{simp} < b_{simp}$:

$$R_l = \frac{\pi}{2} \cdot R_s \cdot N^2 \cdot \sqrt{\xi_0^2 + 1} \cdot \left[(2 + \xi_0^2) \cdot \operatorname{arcsinh}\left(\frac{1}{\xi_0}\right) - \sqrt{\xi_0^2 + 1} \right] \tag{4.17}$$

where R_s is defined as:

$$R_s = \frac{1}{\sigma\delta} \tag{4.18}$$

with σ being the conductivity of copper, and δ the skin depth in copper at 2MHz.

4.2.6 DeVore Equations

This section lists the equations used for simulation from the DeVore paper [15].

Conductor Resistance

The conductor resistance R_l is defined using the DeVore method, as seen in Eq. A15, from [15].

$$R_l = n\sqrt{\frac{\pi f \mu_0}{\sigma}} \cdot \frac{a_{DeVore}}{b_{DeVore}} \left(1 + \frac{R_p}{R_0}\right) \tag{4.19}$$

where $\frac{R_p}{R_0} \approx 0$

Antenna Inductance

The inductance L of the antenna windings with a ferrite core is determined as per Eq. A8 from [15].

$$L = \mu_0 \cdot \frac{n^2}{l} \cdot \left(\pi a_{DeVore}^2\right) \cdot (1 - D) \left[1 + (1 - D_F) \frac{l_F}{l} \cdot \left(\frac{a_F}{a_{DeVore}}\right)^2 \cdot \frac{\kappa' - 1}{1 + D_F (\kappa' - 1)}\right] \tag{4.20}$$

Core Loss Resistance

The core loss resistance R_F is described by Eq. A9 from [15].

$$R_F = \omega \mu_0 \frac{n^2}{l} \cdot \left(\pi a_{DeVore}^2\right) \cdot (1 - D) \cdot (1 - D_F) \cdot \frac{l_F}{l} \cdot \left(\frac{a_F}{a}\right)^2 \cdot \frac{\kappa''}{(\kappa')^2} \cdot \left[\frac{\kappa'}{1 + D_F (\kappa' - 1)}\right]^2 \tag{4.21}$$

Radiation Resistance

The radiation resistance R_r is described by Eq. A14 from [15].

$$R_r = 20 \cdot k^4 \cdot \left(n \pi a_{DeVore}^2\right)^2 \left[1 + \frac{(\kappa' - 1) \cdot (1 - D) \cdot \frac{l_F}{l} \cdot \left(\frac{a_F}{a_{DeVore}}\right)^2}{1 + D_F (\kappa' - 1)}\right]^2 \tag{4.22}$$

Demagnetization Factor

The demagnetization factors $D(l)$ and $D_F(l_F)$ for static fields are given by Eqs. A16a-c from [15].

$$D = \frac{a_{DeVore}^2}{2 \left(\frac{l}{a}\right)^2 e^3} \left[ln\left(\frac{1 + e}{1 - e}\right) - 2e\right] \tag{4.23}$$

for $e^2 > 0$.

$$D = \frac{1}{3}, e^2 = 0 \tag{4.24}$$

$$D = \frac{a_{DeVore}^2}{\left(\frac{l}{2}\right)^2 |e|^3} \left[|e| - tan^{-1}(|e|)\right] \tag{4.25}$$

for $e^2 < 0$ where Eq. A17 in [15] defines e as

$$e^2 \equiv 1 - \left(\frac{2 a_{DeVore}}{l}\right)^2 \tag{4.26}$$

4.3 Simulations

After the MATLAB scripts were written to implement both the Simpson and DeVore models, the simulations were checked by reproducing the results found in both papers. After obtaining the same results, the old transmitter antenna (air core) was simulated to determine the efficiency η to match. The parameters were then varied to determine a new antenna design based upon introduction of a ferrite core.

The simulation of the old, air core antenna had these parameters:

- Air core, $\kappa_m = 1$
- 85 turns of AWG #26 Wire
- 64.4mm per cube face $\rightarrow 2.67x10^{-4}m^3$ Volume

After simulating with these parameters, the efficiencies were determined. These efficiency values are used as the efficiency goal for the new antenna. From the simulation, the efficiency and bandwidth results for both models are:

$\eta_{DeVore} = 2.2896\text{x}10^{-10}$, $BW_{DeVore} = 875Hz$

$\eta_{Simpson} = 2.6554\text{x}10^{-11}$, $BW_{Simpson} = 7,544Hz$

Note the extremely low efficiencies which are common for extremely small (radius $<<$ λ) antennas, and the large difference between the models outcomes owing just to the different approximations used in each. This outcome underscores the fact that this design procedure can only be considered a broad brush guide.

Next the variation of parameters took place, such as various ferrite core materials, volume reduction, varying the number of wire turns, etc., limiting the parameters to those of commercially available materials where applicable. Within the range of commercially available materials, the new antenna parameters were determined to be the following:

Ferrite core: Ferroxcube 4C65, $\kappa_m = 125$, $\tan(\delta) = 0.01$ @ $3MHz$

Volume: $1.4349\text{x}10^{-5}m^3$, or $\approx$ 24.3mm per cube face

$N = 23$ turns of AWG #26 wire

$R_{r_{DeVore}} = 7.3307\text{x}10^{-11}\Omega$

$R_{r_{Simpson}} = 2.3495\text{x}10^{-11}\Omega$

$\eta_{DeVore} = 7.8193\text{x}10^{-11}$, or 34% of previous simulated antenna

$\eta_{Simpson} = 2.5125\text{x}10^{-11}$, or 95% of previous simulated antenna

$BW_{DeVore} = 1,437Hz$, or 164% of previous simulated antenna

$BW_{Simpson} = 4,472Hz$, or 60% of previous simulated antenna

$L_{DeVore} = 46.53\mu H \leftrightarrow C_{res} = 18.51nF$

$L_{Simpson} = 33.28\mu H \leftrightarrow C_{res} = 25.88nF$

The above values were used with one slight change: the cube dimension went from $l = 24.3mm \rightarrow l = 24mm$ for ease of machining and reduction of waste. The antenna was built with these parameters, as described in Section 4.4.

4.4 Antenna Assembly

The transmitter antenna consists of two windings as described in the following sections; a receiver antenna consists of just the inner loop. Fig. 4.5 depicts a model for the transmitter antenna, showing the inner loop and resonant capacitor C_{res} along with the impedance matching loop.

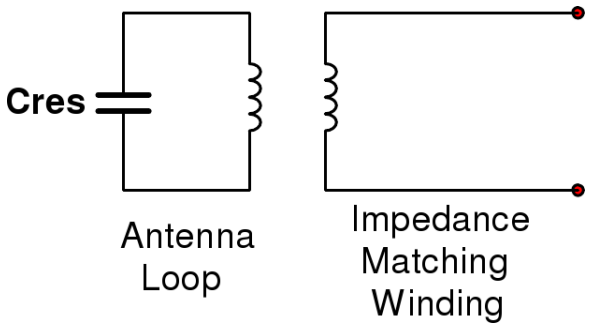

Figure 4.5: Two Loop Antenna Model

A summary of antenna design parameters is as follows:

1. Ferrite: 4C65 from FerroxCube, machined to size by Elna Magnetics
2. Cube dimension: 24mm x 24mm x 24mm $\rightarrow$ 24mm^3
3. Inner loop: 23 turns of #26 enamel wire
4. Impedance matching loop: 3 turns of #26 enamel wire

The first step in fabricating the new antenna was to obtain the machined ferrite blocks from Elna Magnetics. An order for a custom machined block of ferrite # 4C65 was placed and the pieces received were epoxied together to form a cube.

4.4.1 Winding the Inner Stage

This section describes the winding of the inner winding stage for the antenna. This is also the only winding stage for the receiver antenna. After completion of this winding, the antenna must be tuned to resonate as described in Section 4.4.2.

The entire ferrite cube was wrapped in one layer of electrical tape to prevent the wire's enamel coating from rubbing off the wire during the antenna lifetime. For the loop winding, the wire was chosen to be AWG #26 enamel/formvar coated wire, and was wrapped $N_1 = 23$ times. The windings were taped down, and the ends were cut and marked for clarity. This was repeated for the two remaining windings, and the antenna looked as depicted in Fig. 4.6. Lastly, then the entire antenna was wrapped in electrical tape and connectors were added to the windings.

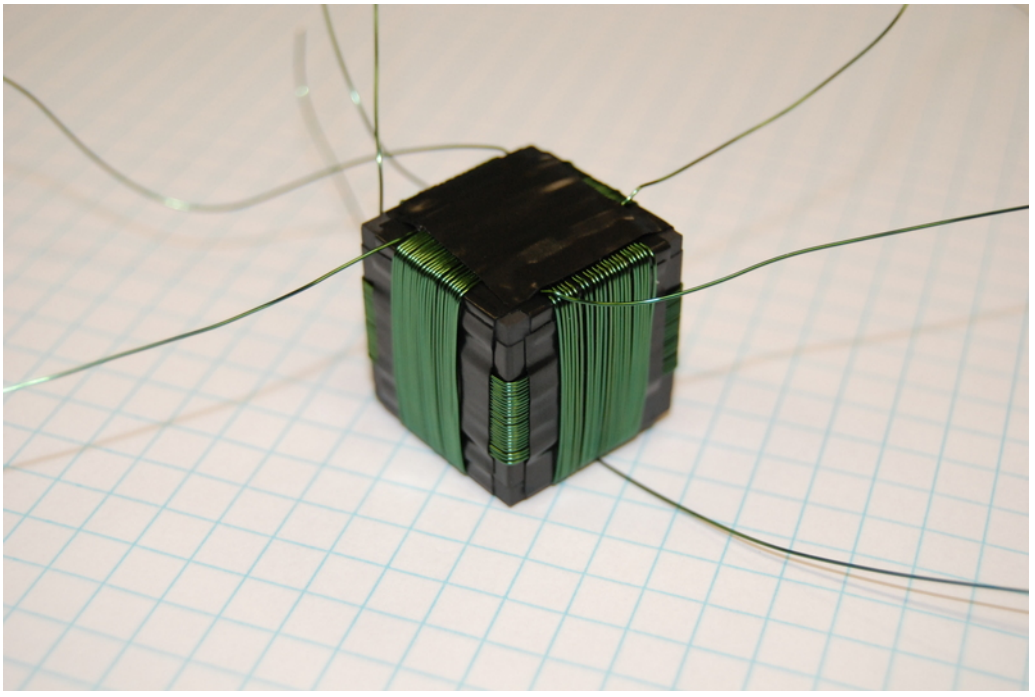

Figure 4.6: Fully Wound Antenna

4.4.2 Resonance Tuning

Every antenna must be tuned to resonate at the desired resonant frequency f_{res}. This was achieved by adding the correct amount of capacitance to have the resonant frequency be at the desired f_{res}.

The transmitter transmits on these three frequencies: $f_1 = 170.2kHz$, $f_2 = 171.5kHz$,

and $f_3 = 172.7kHz$, hence the desired resonant frequency is approximately $f_2 = 171.5kHz$. To calculate the necessary tuning capacitors, we use Eq. 4.27.

$$f_{res} = \frac{1}{2\pi\sqrt{LC_{res}}} \tag{4.27}$$

where L = inductance of the antenna loop, C_{res} = resonance capacitor, and f_{res} = desired resonance frequency.

For this antenna, the inductance was measured and found to be approximately $L \approx 50\mu H$, comparing quite well with the DeVore based prediction of $46.53\mu H$. This was calculated by using a known valued capacitor and finding f_{res} with the bench equipment, then working backwards to find L. This value of L is more accurate than that obtained with an inductance meter as the inductance of the antenna depends on the exciting frequency, due to the effects of a ferrite core.

So, for $f_{res} = 171.5kHz$, Eq. 4.27 yields:

$$f_{res} = \frac{1}{2\pi\sqrt{LC_{res}}} \rightarrow C_{res} = \frac{1}{L \cdot (2\pi f_{res})^2} \rightarrow \frac{1}{50\mu H \cdot (2\pi 171.5kHz)^2} \rightarrow C_{res} = 17.2nF$$

The result was treated as a ballpark value, not an exact value, since there are errors in measuring the real inductance due to variations in capacitors owing to non-zero value tolerances. This dictated starting with a ballpark value of $C_{res} = 15nF$ and using bench equipment to help determine the exact capacitor combination needed as described below.

On the bench, a test signal of $f = 171.5kHz$ drove a loop wire to excite the antenna, and the antenna was connected to an oscilloscope. The test signal's frequency was adjusted to find the resonant frequency of the antenna, and capacitance was added to reduce the resonant frequency or capacitance was removed to increase the resonant frequency, until the antenna resonated at $f_{res} = 171.5kHz$. This procedure was repeated until all three antenna loops were tuned.

Once the antenna was tuned, these particular capacitors were soldered onto the antenna connectors. When a receiver antenna was being built, these capacitors were installed on the corresponding Mantenna RF Front End board.

4.4.3 Impedance Matching Loop

The impedance matching loop must be optimized to match the impedance of the antenna with that of the amplifier stage to yield maximum power transfer. This match can

be determined by monitoring the voltage across the inner loop, as observed at the capacitor C_{res}, as the ratio of the turns in both loops is varied; the goal is maximization of this voltage.

The number of impedance matching wire turns was obtained by trial and error since the electromagnetics involved in such a sparsely wound transformer are difficult to account for without creating another design project. Table 4.1 contains a summary of the voltages observed across the inner loop capacitor C_{res} while varying the number of impedance matching turns N_2.

Table 4.1: Windings versus Voltage for Impedance Matching Loop

# Turns	V_{pk-pk}
$1\ \frac{1}{4}$	$\approx$ 37.50 Volts
$2\ \frac{1}{4}$	$\approx$ 60.94 Volts
$2\ \frac{1}{2}$	$\approx$ 107.8 Volts
3	$\approx$ 117.2 Volts
$3\ \frac{1}{4}$	$\approx$ 117.2 Volts
$3\ \frac{1}{2}$	$\approx$ 117.2 Volts
$3\ \frac{3}{4}$	$\approx$ 117.2 Volts
$4\ \frac{1}{4}$	$\approx$ 104.7 Volts
$6\ \frac{1}{4}$	$\approx$ 79.69 Volts

From table 4.1, the optimal number of windings is $N_2 = 3$ turns for the impedance matching loop. This loop was installed on each of the three loop antennas. The new antennas was now ready to be used with the transmitter to which it has been matched.

4.5 Results

Here we summarize the outcomes of the design and implementation including performance of the new antenna within the mantenna system after assembly.

Regarding the physical size: the length of each cube face was reduced from $l = 64.4mm$ to $l = 24mm$. That is, the new antenna length, l, is 36% of previous antenna's length. This corresponds to a volume reduction from $V = 2.67\text{x}10^{-4}m^3$ to $V = 1.38\text{x}10^{-5}m^3$; the new antenna's volume V is 19% of previous volume.

Measuring the bandwidth, it was observed that the new antenna has a bandwidth of $BW = 13.8kHz$. This is greater than the minimum $4kHz$ of bandwidth that is required by the mantenna transmitter system.

In addition, the electronics were reworked and a new printed circuit board was fab-

ricated. Paired with a smaller sized battery and the new antenna, this resulted in the system being reduced substantially in size.

Fig. 4.7 serves to illustrate the changes in the transmitter system. The transmitter implementation changed from what is seen in Fig. 4.7(a) to what is seen in Fig. 4.7(b), with the latter being a much more practical system for use by firefighters as it is significantly smaller in size while maintaining the performance of the previous system.

(a) Old Transmitter System (b) New Transmitter System

Figure 4.7: Transmitter System Change

The overall antenna performance was experimentally verified as having been preserved by placing the old transmitter and new transmitter at a fixed distance and measuring the received signal strength at the receiver. It was found that the received signal amplitude of the new transmitter was within 96% (or -0.35dB) of the previous transmitter's resulting received signal. This is close enough to the original transmitter's performance that there should be little homing system performance degradation observed when compared against the old transmitter system.

The small form factor of this new antenna was so advantageous that it was quickly investigated as a replacement for the receiver antenna system. The old receiver antenna setup consisted of three ferrite rod antennas placed orthogonally, one for each axis; this delicate, sizeable setup was prone to breakdowns. The new antenna's cube shape resulted in a significantly improved physical profile and more reliable receiver antenna system, and its performance was found to be on par with the ferrite rod antennas. Thus, the new antenna design is in use on the transmitter and receiver sides.

Fig. 4.8 shows the old and the new receiver antenna system. The receiver wand's antenna went from what is seen in Fig. 4.8(a) to what is seen in Fig. 4.8(b), with the latter a much smaller and more reliable antenna system.

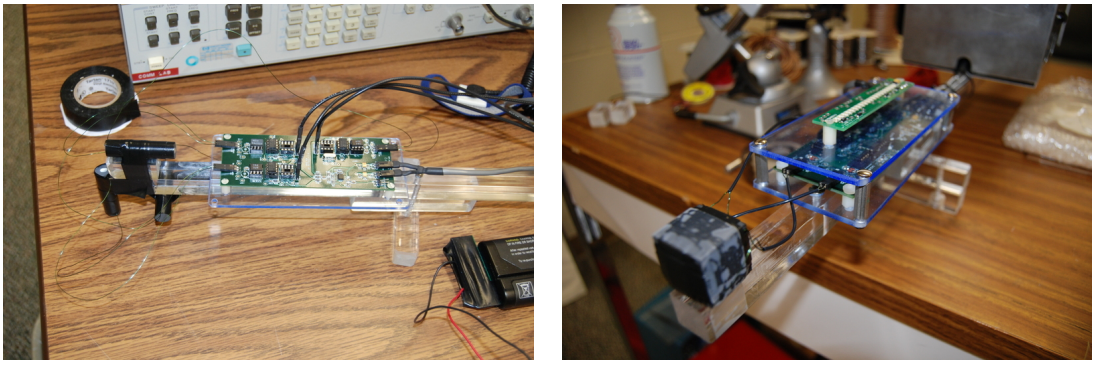

(a) Old Receiver Antenna Setup

(b) New Receiver Antenna Setup

Figure 4.8: Receiver Antenna Change

Chapter 5

Near Field RF Data Capture

During a PPL test held at the Bartlett Center in June 2008, a newly constructed building on the WPI Campus, the PPL system performed surprisingly poorly. The exact cause of the high multipath observed was unclear, but building construction, such as energy efficient glass panels (glass coated with UV/IR blocker), prefabricated brick panels, etc. are most likely the reason for poor performance. From this poor performance, it was noted that the PPL's radiation far field approach would need a significant breakthrough to perform well in a building with modern building materials. Fig. 5.1 depicts the WPI Bartlett Center, and greenish-blue color of the glass in Fig. 5.1(b) clearly shows the energy efficient coating used.

(a) Bartlett Center Front (b) Bartlett Center Rear

Figure 5.1: WPI Bartlett Center

During this test, the Mantenna was also tested and appeared to perform as normally seen in other buildings; targets placed inside the building were detected with little performance degradation from the exterior when perimeter searches were performed (when in

range), and inside the targets were located with ease.

In addition, a range test was performed with the Mantenna transmitter placed on both sides of one of the large coated glass windows to determine what detrimental effect, if any, the coating had on the Mantenna's performance. The transmitter was placed on one side of the large glass window on the rear side of the building (the side facing the quadrangle). The receiver wand was then placed directly outside the window, and the distance was slowly increased until the signal was no longer detectable. This was then repeated with the transmitter being placed directly inside the large glass pane.

For the transmitter located directly outside of the glass pane, the range obtained with the receiver wand was 13.423 meters, while the range with the transmitter on the inside of the glass was 14.130 meters. The slight increase in range with the transmitter being inside is thought to be due to the coupling of the transmitter's field with the steel in the building. This test showed the Mantenna's Near Field approach has potential to work in a harsh RF environment where the PPL system's radiation far field approach is significantly hampered.

The next step was to determine if the Near Field approach could be enhanced to work as a Location and Tracking rescue system, as a potential supplement or replacement for the radiation far field approach. Fig. 5.2 depicts a Near Field Location System with a transmitter of unknown position and unknown orientation surrounded by receivers of fixed position and orientation. In order to achieve the concept system described in Fig. 5.2, the simpler case of obtaining a position estimate with an unknown transmitter orientation must first be solved. The simpler case was explored using a minimal configuration of one transmitter and one receiver as described in Section 5.1. This minimal configuration was sufficient to develop the theory and tools necessary towards developing a complete NFL prototype as depicted in Fig. 5.2.

For the minimal configuration test, the received signal obtained with one Mantenna in the near field as a function of transmitter position would need to be collected for further analysis. Professor Cyganski and the author agreed to a round of data collection by the Mantenna team to capture the received signal function while Professor Cyganski did some theoretical explorations regarding a near field location and tracking system. Alden Hall at WPI was chosen as the site for the next set of Mantenna tests, with the captured data analyzed against the theoretical received signal function predicted by the approximate near field antenna coupling equations.

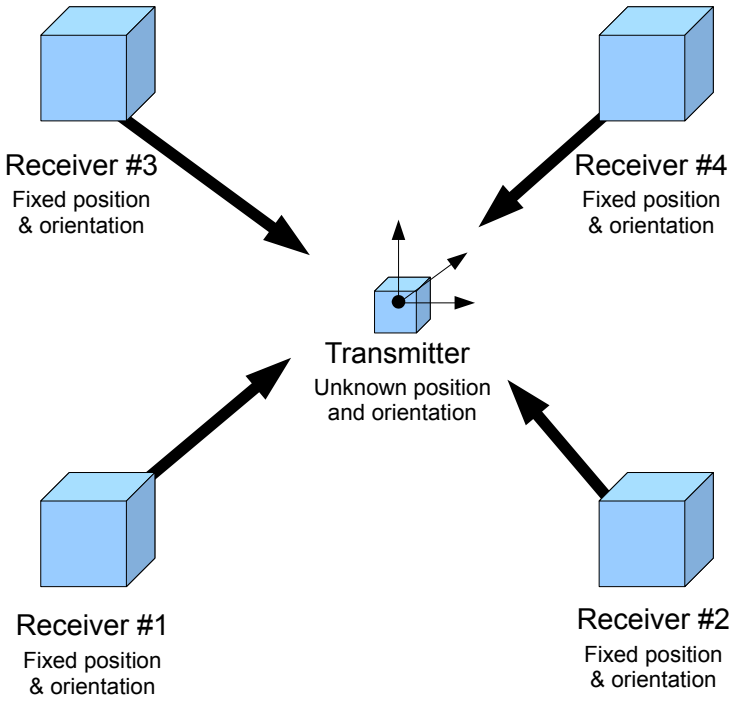

Figure 5.2: Near Field Location System Concept

5.1 Alden Hall Data Capture

The Alden Hall data collection was set up as depicted in Fig. 5.3. In Alden Hall, a 31 foot by 31 foot grid was marked on the floor. The Mantenna receiver Wand's position and orientation were fixed at one corner, and the Transmitter was moved about the grid while its orientation was kept fixed. The receiver captured data for the 961 different transmitter locations along the grid. This was sufficient to capture the Near Field received signal function for one quadrant, as the receiver Wand was fixed at one corner. It was determined that the four quadrants would be symmetrical, thus data was collected for one quadrant in detail.

After the necessary MATLAB scripts were written to process the data, the data was plotted. These plots were subsequently compared against Professor Cyganski's Maple script which computed the approximate antenna coupling equations and produced the theoretical received signal function. The Maple model was written to mimic the test setup of the Alden Hall data capture. The Maple model assumes one carrier transmitted by the transmitter on the Z-axis with the receiver wand receiving on all three axes (the Mantenna Transmitter transmits on three axes; ignoring two of the three transmitter axes allows for direct comparison against the Maple code). A detailed explanation of the Maple code's

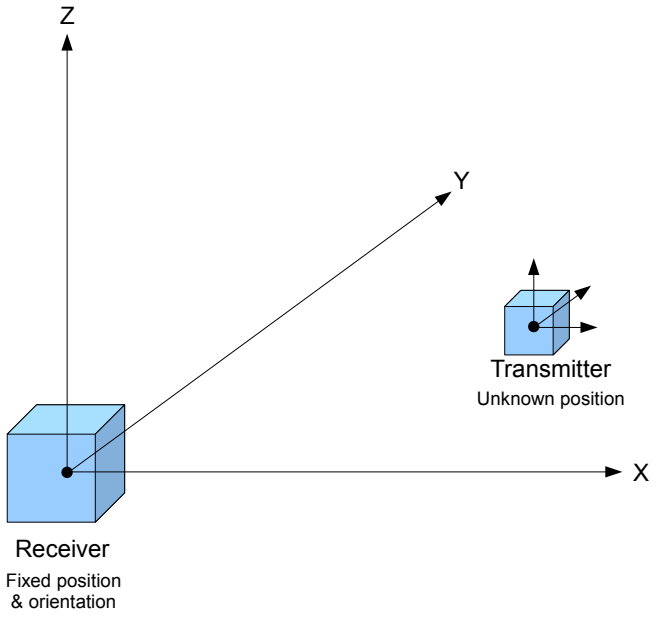

Figure 5.3: Alden Hall Test Geometry Reference

model is in Chapter 6, where the theory is built to describe the Near Field Location System.

The amplitude of the received signal data obtained by the Mantenna Wand's front antenna for a single transmitter frequency is plotted alongside the theoretical function predicted by Maple in Figs. 5.4, 5.5, and 5.6. The longitudinal/on-axis antenna data is seen first in Fig. 5.4, the transverse/horizontal antenna data is seen in the next Fig. 5.5, and the up/down or vertical antenna data is seen in the final Fig. 5.6.

In Fig. 5.4, we see the X-axis data. The captured RF of Fig. 5.4(a) and the Maple predicted RF of Fig. 5.4(b) are similar and seem to substantially match.

In Fig. 5.5, we see the Y-axis data. The captured RF of Fig. 5.5(a) and the Maple predicted RF of Fig. 5.5(b) don't quite match. Fig. 5.5(b) predicts no RF signal, while we see some in the captured RF of Fig. 5.5(a). It's significant to note that the amplitude of the received signal is significantly less for this antenna than the other two antennas, leading one to believe the observed values are due to leakage between otherwise independent antenna modes due to unavoidable physical imperfections in the antenna construction.

In Fig. 5.6, we see the Z-axis data. The captured RF of Fig. 5.6(a) and the Maple predicted RF of Fig. 5.6(b) are similar and seem to substantially match.

From this, it was decided that the equations from Maple would be written in MATLAB to take advantage of MATLAB's signal processing capabilities. Once the received signal

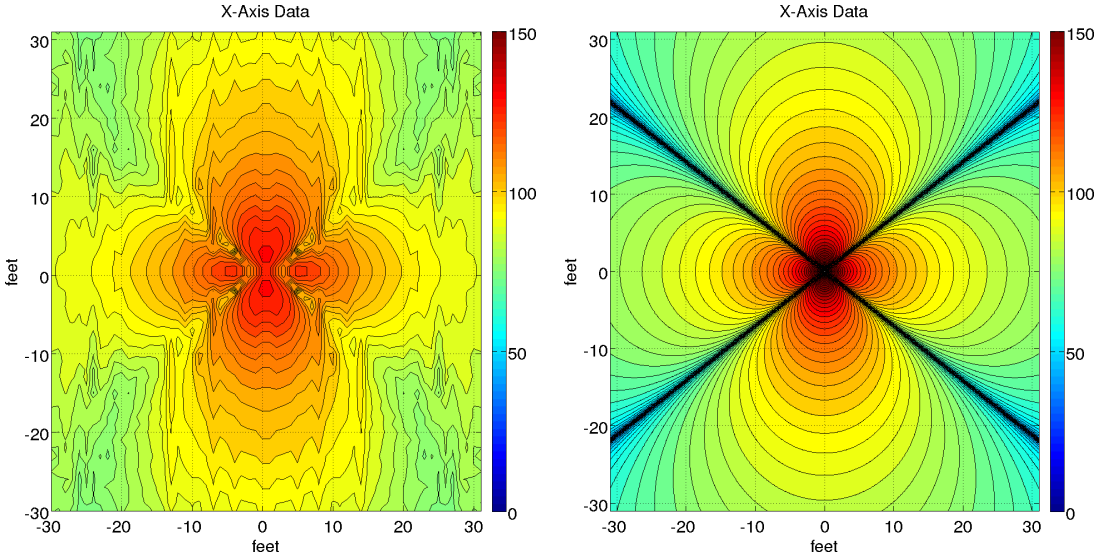

(a) Alden Data $20\log_{10}|H|$ (b) Analytic Data $20\log_{10}|H|$

Figure 5.4: X-Axis Antenna RF Data

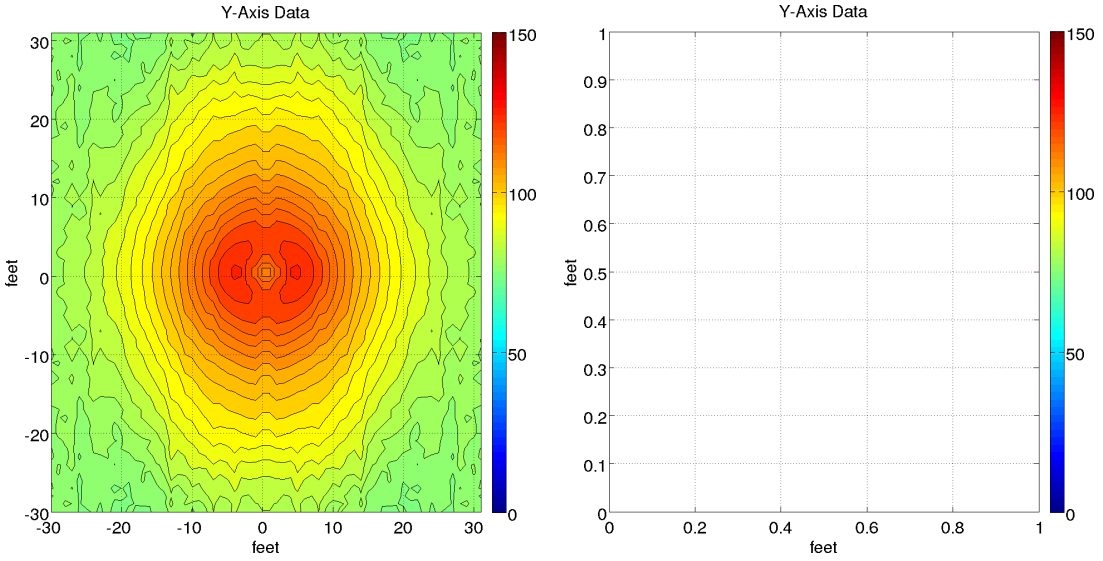

(a) Alden Data $20\log_{10}|H|$ (b) Analytic Data $20\log_{10}|H|$

Figure 5.5: Y-Axis Antenna RF Data

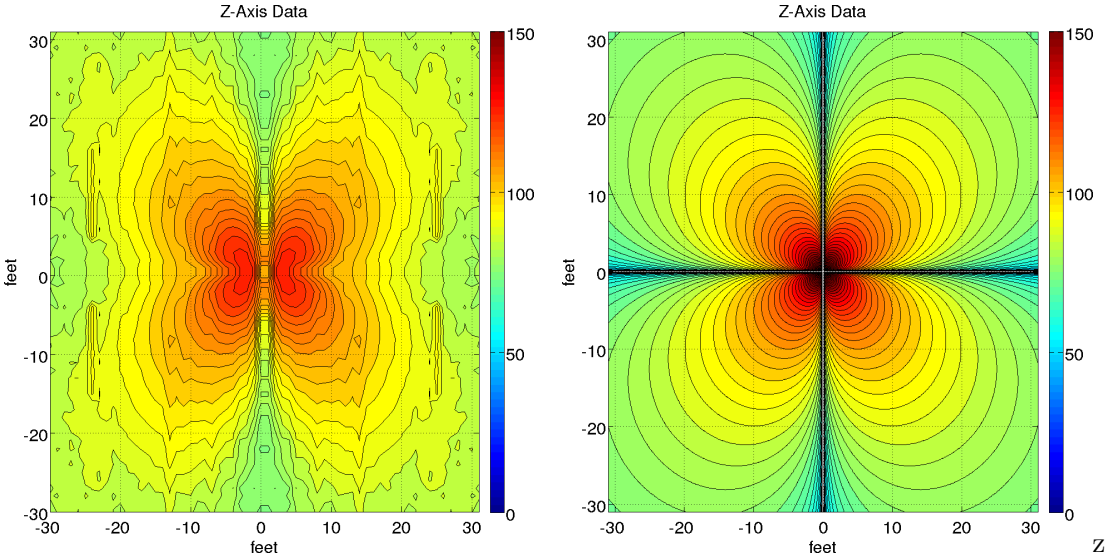

(a) Alden Data $20\log_{10}|H|$ (b) Analytic Data $20\log_{10}|H|$

Figure 5.6: Z-Axis Antenna RF Data

function equations were in a MATLAB script, a search algorithm would be implemented to find a position estimate based on Mantenna Wand received signal data for an "unknown" location.

Chapter 6

Near Field Location System

This chapter describes the development of the Near Field Location system theory and software implementation. The theory starts with the equations that describe the fields from a loop antenna, then describes how to generate projections and functions to find the amplitude at an antenna with any orientation and any distance from the source. After the synthetic RF data is generated, the effective orientation of the transmitter is varied by computationally rotating the data. Then the search metric to find the best position estimate is discussed.

6.1 Near Field Projections

We start with the **E** and **H** equations that completely describe a small loop antenna, given in Section 2.1:

$$\begin{aligned} H_r &= j\frac{ka^2 I_0 \cos(\theta)}{2r^2}\left[1+\frac{1}{jkr}\right]e^{-jkr} \\ H_\theta &= -\frac{(ka)^2 I_0 \sin(\theta)}{4r}\left[1+\frac{1}{jkr}-\frac{1}{(kr)^2}\right]e^{-jkr} \\ H_\phi &= 0 \\ E_r &= E_\theta = 0 \\ E_\phi &= \eta\frac{(ka)^2 I_0 \sin(\theta)}{4r}\left[1+\frac{1}{jkr}\right]e^{-jkr} \end{aligned} \tag{6.1}$$

Now we need to extract the magnitude of the field as received by each antenna for all points in the x-y plane. We accomplish this by taking the projection of the field for each of the three receiver axes. The projections give the magnetic field at every point in the

x-y plane, and is an approximation of what would be sensed by a parallel loop if only the central magnetic coupling is assumed with no other field components acting (the antenna coupling reciprocity integral would have to be evaluated to get the exact coupling).

With the help of Maple, using the sptocart, map, evalf, and unapply commands, and evaluating Eq. 6.1 for $I_0 = 1$, $k = 2\pi$, and a loop with area $\frac{1}{4\pi^2}$. The spatially scaled (one unit of distance equals one wavelength) magnitude of the x-component of the **H** field parallel to the loop normal is given as in Eq. 6.2

$$X_{\text{projf}} = \frac{0.002015720901}{\left(x^2+y^2+z^2\right)^3}\cdot\left(\begin{array}{c} 9.0x^2+9.0y^2+9.0z^2+118.4352528z^4+236.8705057y^2x^2 \\ +236.8705057x^2z^2+236.8705057z^2y^2+118.4352528y^4 \\ +118.4352528x^4+1558.545457x^6+1558.545457y^6 \\ +1558.545457z^6+9351.272744z^2y^2x^2+4675.636372y^2x^4 \\ +4675.636372z^2x^4+4675.636372y^4x^2+4675.636372z^4x^2 \\ +4675.636372z^2y^4+4675.636372z^4y^2 \end{array}\right)^{\frac{1}{2}} |zx| \tag{6.2}$$

Now, the magnitude of the y-component of the **H** field parallel to the loop normal is seen in Eq. 6.3.

$$Y_{\text{projf}} = \frac{0.002015720901}{\left(x^2+y^2+z^2\right)^3}\cdot\left(\begin{array}{c} 9.0x^2+9.0y^2+9.0z^2+118.4352528z^4+236.8705057y^2x^2 \\ +236.8705057x^2z^2+236.8705057z^2y^2+118.4352528y^4 \\ +118.4352528x^4+1558.545457x^6+1558.545457y^6 \\ +1558.545457z^6+9351.272744z^2y^2x^2+4675.636372y^2x^4 \\ +4675.636372z^2x^4+4675.636372y^4x^2+4675.636372z^4x^2 \\ +4675.636372z^2y^4+4675.636372z^4y^2 \end{array}\right)^{\frac{1}{2}} |zy| \tag{6.3}$$

Finally, the magnitude of the z-component of the **H** field parallel to the loop normal

is seen in Eq. 6.4.

$$Z_{\text{projf}} = \frac{0.002015720901}{(x^2+y^2+z^2)^{5/2}} \cdot \left(\begin{array}{l} 1558.545457x^8 - 39.47841762x^6 - 39.47841762y^6 \\ +1558.545457y^8 - 118.4352528y^4x^2 + 1558.545457z^4x^4 \\ +157.9136705z^4x^2 + 1558.545457z^4y^4 + 3117.090915z^2y^6 \\ -39.47841762z^2y^4 + 157.9136705z^4y^2 + 6234.181829y^2x^6 \\ +3117.090915z^2x^6 + 9351.272744y^4x^4 - 118.4352528y^2x^4 \\ -39.47841762z^2x^4 + 6234.181829y^6x^2 \\ +9351.272744z^2y^4x^2 + 9351.272744z^2y^2x^4 + x^4 \\ +3117.090915y^2z^4x^2 - 78.95683523z^2y^2x^2 + y^4 \\ +2.0x^2y^2 + 4.0z^4 - 4.0x^2z^2 - 4.0y^2z^2 + 157.9136705z^6 \end{array} \right)^{\frac{1}{2}} \tag{6.4}$$

The field equations are expressed in terms of wavelength. To put this into feet, we use the scalar scalefoot $= \frac{\frac{1}{3}}{\lambda} = \frac{\frac{1}{3}}{1600}$ to convert from wavelength to feet. This scalar is used when plotting the equations to give the correct scaling.

Plotting the projection equations for all three axes describes the appropriate received signal amplitudes for that orientation. Plotting the equations on a log scale, as well as in feet instead of wavelengths by using the above mentioned scale factor, shows how the Near Field behaves within the specified distance from the source.

A graph of the x-component, Eq. 6.2, is seen in Fig. 5.4(b). A graph of the y-component, Eq. 6.3, is seen in Fig. 5.5(b). There is no field in the case of the Y component, so the plot in Fig. 5.5(b) is expected to be blank. A graph of the z-component, Eq. 6.4, is seen in Fig. 5.6(b).

Eqs. 6.2, 6.3, and 6.4 describe the received signal function seen by each of the Mantenna receiver wand's three axes (x, y, and z) for a Mantenna Transmitter transmitting on the Z-axis, as described earlier in Section 3.2. In order to achieve the omni-directional field coverage the Mantenna Transmitter transmits on all three axes (x, y and z). Using a different transmit frequency for each transmitter axis is required to obtain the uniform field pattern, as the same frequency would create nulls at various points. In addition, it is advantageous as it allows for signal processing of the receiver wand's data to discriminate which signals at each of the receiver wand's axes are associated with which transmitter frequency and corresponding axes, as described in Section 3.2.

6.2 Varying Orientations of the Transmitter

Section 6.1 describes how the received signal function for the transmitter and receiver is obtained. However, these are only valid for one particular orientation of the source. To compute the fields for various orientations of the transmitter about the X, Y and Z axes as seen by the receiver, rotation matrices are used instead of re-deriving the field equations directly as functions of angles.

Say the receiver wand's received signal data is collected and assembled in a 3x3 matrix. Each column corresponds to the received signal data for one of the three transmitter's axes (and hence one frequency), and each row corresponds to the data seen by the wand's x-axis, y-axis, and z-axis. This data assembled in the matrix $\mathbf{F}$ would be composed as per Eq. 6.5.

$$\mathbf{F} = \begin{bmatrix} a_1\hat{x} & a_2\hat{x} & a_3\hat{x} \\ b_1\hat{y} & b_2\hat{y} & b_3\hat{y} \\ c_1\hat{z} & c_2\hat{z} & c_3\hat{z} \end{bmatrix} \tag{6.5}$$

where a_1 is the signal observed by the receiver wand's x-axis for the first transmitter frequency, b_1 is the signal observed by the receiver wand's y-axis for the first transmitter frequency, c_1 is the signal observed by the receiver wand's z-axis for the first transmitter frequency, etc. Thus, a matrix $\mathbf{F}$ consisting of nine data points completely describes the received signal function for the Mantenna at any given x-y location for the given transmitter orientation.

Suppose $\mathbf{F_1}$ is a matrix consisting of the received signal data for a given point in the x-y plane. To find a rotation $\mathbf{F_1'}$ of $\mathbf{F_1}$, we assemble the matrix $\mathbf{F_1}$ and multiply it by the rotation matrix $\mathbf{R}$ to get $\mathbf{F_1'}$, as seen in Eq. 6.6.

$$\mathbf{F_1'} = \mathbf{R}\mathbf{F_1}$$

$$\mathbf{F_1'} = \begin{bmatrix} a_1' & a_2' & a_3' \\ b_1' & b_2' & b_3' \\ c_1' & c_2' & c_3' \end{bmatrix} = \mathbf{R} \begin{bmatrix} a_1 & a_2 & a_3 \\ b_1 & b_2 & b_3 \\ c_1 & c_2 & c_3 \end{bmatrix} \tag{6.6}$$

The choice of the rotation matrix $\mathbf{R}$ in Eq. 6.6 depends on the desired axis of rotation. For a rotation about the X-axis we define the angle of rotation as θ, for a rotation about the Y-axis we define the angle of rotation as ϕ, and for a rotation about the Z-axis we

define the angle of rotation as ψ. In general form, the rotation matrix for the x-axis as a function of θ is given by Eq. 3.3 in [18]:

$$\mathbf{R}_{\mathbf{x},\theta} = \begin{bmatrix} 1 & 0 & 0 \\ 0 & \cos(\theta) & \sin(\theta) \\ 0 & -\sin(\theta) & \cos(\theta) \end{bmatrix} \tag{6.7}$$

The rotation matrix for the y-axis as a function of ϕ is given by Eq. 3.2 in [18]:

$$\mathbf{R}_{\mathbf{y},\phi} = \begin{bmatrix} \cos(\phi) & 0 & -\sin(\phi) \\ 0 & 1 & 0 \\ \sin(\phi) & 0 & \cos(\phi) \end{bmatrix} \tag{6.8}$$

The rotation matrix for the z-axis as a function of ψ is given by Eq. 3.1 in [18]:

$$\mathbf{R}_{\mathbf{z},\psi} = \begin{bmatrix} \cos(\psi) & \sin(\psi) & 0 \\ -\sin(\psi) & \cos(\psi) & 0 \\ 0 & 0 & 1 \end{bmatrix} \tag{6.9}$$

Thus, one can obtain the effect of any arbitrary rotation of the transmitter by inserting the appropriate angles θ, ϕ, and ψ into the appropriate rotation matrix $\mathbf{R}$ and multiplying the data point by the matrix to get the desired orientation.

6.3 Orientation Independent Position Estimate

Section 6.1 described how to obtain the received signal function for all three axes of the source for a particular transmitter orientation, and Section 6.2 described how to obtain the received signal function for any arbitrary transmitter orientation. This section will describe how to obtain an accurate x-y position estimate given the received signal data and any transmitter orientation without having to directly compare the received data against all possible transmitter rotations.

Suppose we have receiver data for an arbitrary point in x-y - say this is chosen randomly from our received signal function, for any arbitrary transmitter orientation, and corrupted with noise. We wish to find the position with the best match to our location data.

We assemble our received data into a matrix as per Eq. 6.10:

$$\mathbf{A} = \begin{bmatrix} x'_1 & x'_2 & x'_3 \\ y'_1 & y'_2 & y'_3 \\ z'_1 & z'_2 & z'_3 \end{bmatrix} \tag{6.10}$$

We assemble the received signal data for each point, using only one transmitter orientation, as a matrix as per Eq. 6.11:

$$\mathbf{B} = \begin{bmatrix} x_1 & x_2 & x_3 \\ y_1 & y_2 & y_3 \\ z_1 & z_2 & z_3 \end{bmatrix} \tag{6.11}$$

The standard method of comparing two matrices and determining the exact rotation matrix $\mathbf{R}$ applied to $\mathbf{B}$ to produce $\mathbf{A}$ is called the Procrustes problem, as seen in Eq. 12.4.1 in [19]. However, this method does not always yield the correct answer when the data is corrupted, such as with noisy data, so another search metric was used.

The paper [20] describes a more robust method of finding the matrix $\mathbf{R}$, and its search metric was used for finding the best position estimate in our implementation. The two matrices are compared as per Eq. 2 from [20], seen in Eq. 6.12:

$$min_R||\mathbf{A}||_F^2 + ||\mathbf{B}||_F^2 - 2\mathrm{tr}\,(DS) \tag{6.12}$$

where S is defined by:

$$S = \begin{cases} I & \text{if } \det(\mathbf{AB^T}) \geq 0 \\ \mathrm{diag}(1, 1, \ldots, 1, -1) & \text{if } \det(\mathbf{AB^T}) < 0 \end{cases}$$

and where $\mathbf{A}$ is the matrix of receiver wand data, $\mathbf{B}$ is the matrix of signal function data for a given x-y position, $||\mathbf{A}||_F$ is the Frobenius norm of the matrix $\mathbf{A}$, and UDV^T is a singular value decomposition of $\mathbf{AB^T}$.

The location where Eq. 6.12 is minimized is the best position estimate in the received signal data, and is the best position estimate of the x-y location of the transmitter. The paper [20] also describes a construction for the rotation matrix $\mathbf{R}$ which applied to $\mathbf{B}$ produces $\mathbf{A}$, but for our purposes this information isn't necessary and thus not implemented.

6.4 MATLAB Numerical Received Signal Function

The next step is the implementation of the methods described by the theory in Sections 6.1, 6.2, and 6.3. Several MATLAB scripts were written to generate the received signal function for the tri-axial transmitter and compute the fields generated by arbitrary rotations of the transmitter. A random spatial point and transmitter orientation were chosen from the synthetic field data was generated to represent the receiver data. Then the position estimate was computed using a two-dimensional search via the minimization of the rotation invariant metric discussed in Section 6.3.

Fig. 6.1 shows a plot of the Numerical Signal Function seen by the receiver wand's X-axis for a transmitter transmitting on the Z-axis. Similarly, the Numerical Signal Function seen by the receiver wand's Y-axis is seen in Fig. 6.2, and the Numerical Signal Function seen by the receiver wand's Z-axis is seen in Fig. 6.3.

Recall from Section 3.2 that the Mantenna uses a tri-axial transmitter. The Numerical Signal Function seen by the receiver wand for a transmitter transmitting on the other two axes at different frequencies is similar to what is seen for Z-axis transmitting case with the signal function seen by each axis swapped appropriately, and the plots are skipped for brevity.

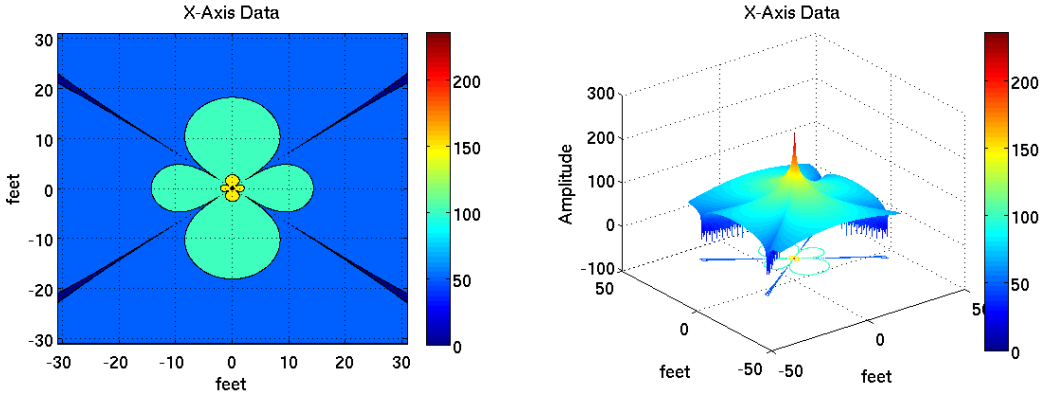

(a) $20\log_{10}|H|$ X-Axis Contour Plot

(b) $20\log_{10}|H|$ X-Axis Mesh Plot

Figure 6.1: Numerical Signal Function X-Axis Plots

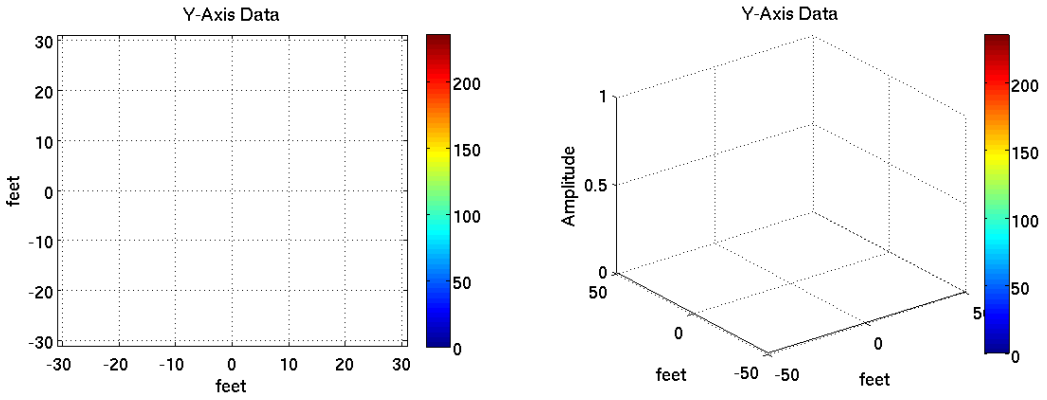

(a) $20\log_{10}|H|$ Y-Axis Contour Plot (b) $20\log_{10}|H|$ Y-Axis Mesh Plot

Figure 6.2: Numerical Signal Function Y-Axis Plots

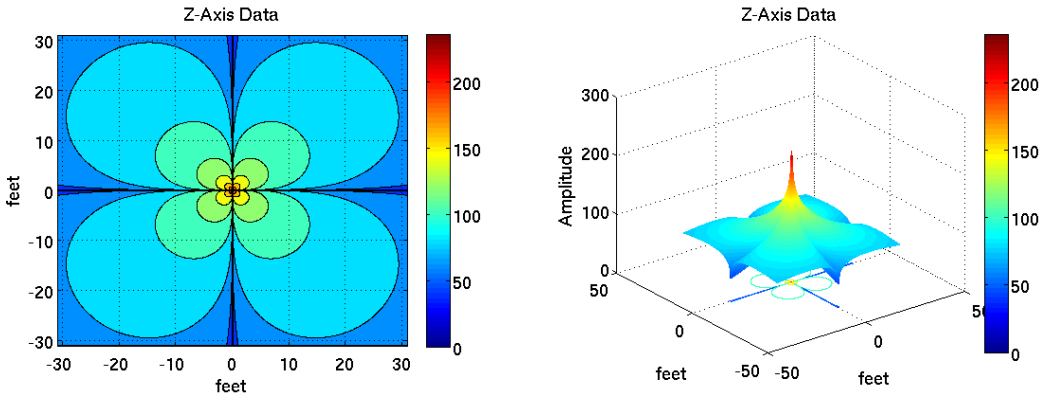

(a) $20\log_{10}|H|$ Z-Axis Contour Plot (b) $20\log_{10}|H|$ Z-Axis Mesh Plot

Figure 6.3: Numerical Signal Function Z-Axis Plots

6.5 Numerical Search Simulations

A MATLAB simulation was executed and the results are described in the following. The numerical received signal function was computed for a 62 foot by 62 foot grid (with 1 foot increments, for a total of 3844 possible points), and the transmitter orientations were mimicked using the rotation angles $\theta = \{0, \frac{\pi}{5}, \frac{2\pi}{5}, \frac{3\pi}{5}, \frac{4\pi}{5}, \pi, \frac{6\pi}{5}, \frac{7\pi}{5}, \frac{8\pi}{5}, \frac{9\pi}{5}, 2\pi\}$, $\phi = \{0, \frac{\pi}{5}, \frac{2\pi}{5}, \frac{3\pi}{5}, \frac{4\pi}{5}, \pi, \frac{6\pi}{5}, \frac{7\pi}{5}, \frac{8\pi}{5}, \frac{9\pi}{5}, 2\pi\}$, and $\psi = \{0, \frac{\pi}{5}, \frac{2\pi}{5}, \frac{3\pi}{5}, \frac{4\pi}{5}, \pi, \frac{6\pi}{5}, \frac{7\pi}{5}, \frac{8\pi}{5}, \frac{9\pi}{5}, 2\pi\}$.

A simulation was executed in which a random point in x-y was chosen along with a random transmitter orientation (θ, ϕ, and ψ) and the position estimate was computed. This simulation was executed 25 times, and the results are in Table 6.1.

Table 6.1: Numerical Signal Function Simulation Results

Truth Data						Position Estimates			
X	Y	Z	θ	ϕ	ψ	X (est)	Y (est)	Z (est)	Correct?
60	15	1	$\frac{6\pi}{5}$	π	$\frac{9\pi}{5}$	60	15	1	Y
48	29	1	0	$\frac{8\pi}{5}$	$\frac{4\pi}{5}$	48	29	1	Y
39	50	1	$\frac{9\pi}{5}$	$\frac{7\pi}{5}$	$\frac{2\pi}{5}$	39	50	1	Y
26	59	1	$\frac{9\pi}{5}$	$\frac{4\pi}{5}$	$\frac{9\pi}{5}$	26	59	1	Y
5	23	1	$\frac{8\pi}{5}$	0	$\frac{\pi}{5}$	5	23	1	Y
14	13	1	$\frac{6\pi}{5}$	$\frac{3\pi}{5}$	$\frac{2\pi}{5}$	14	13	1	Y
2	47	1	$\frac{4\pi}{5}$	$\frac{9\pi}{5}$	π	2	47	1	Y
27	53	1	π	$\frac{2\pi}{5}$	$\frac{7\pi}{5}$	27	53	1	Y
53	2	1	$\frac{7\pi}{5}$	$\frac{4\pi}{5}$	$\frac{8\pi}{5}$	53	2	1	Y
32	45	1	$\frac{4\pi}{5}$	$\frac{3\pi}{5}$	$\frac{2\pi}{5}$	32	45	1	Y
13	43	1	$\frac{3\pi}{5}$	π	$\frac{2\pi}{5}$	13	43	1	Y
44	24	1	$\frac{9\pi}{5}$	$\frac{9\pi}{5}$	$\frac{6\pi}{5}$	44	24	1	Y
32	57	1	$\frac{8\pi}{5}$	$\frac{6\pi}{5}$	$\frac{8\pi}{5}$	32	57	1	Y
42	22	1	$\frac{3\pi}{5}$	$\frac{3\pi}{5}$	π	42	22	1	Y
46	20	1	$\frac{8\pi}{5}$	$\frac{6\pi}{5}$	$\frac{4\pi}{5}$	46	20	1	Y
45	35	1	$\frac{4\pi}{5}$	$\frac{7\pi}{5}$	$\frac{6\pi}{5}$	45	35	1	Y
50	60	1	π	$\frac{9\pi}{5}$	$\frac{2\pi}{5}$	50	60	1	Y
62	18	1	$\frac{3\pi}{5}$	$\frac{9\pi}{5}$	$\frac{7\pi}{5}$	62	18	1	Y

Continued on next page

Table 6.1 – continued from previous page

Truth Data						Position Estimates			
X	Y	Z	θ	ϕ	ψ	X (est)	Y (est)	Z (est)	Correct?
9	2	1	$\frac{9\pi}{5}$	$\frac{2\pi}{5}$	$\frac{3\pi}{5}$	9	2	1	Y
42	19	1	π	$\frac{\pi}{5}$	0	42	19	1	Y
37	27	1	π	$\frac{3\pi}{5}$	$\frac{4\pi}{5}$	37	27	1	Y
15	37	1	$\frac{8\pi}{5}$	π	$\frac{6\pi}{5}$	15	37	1	Y
14	25	1	$\frac{8\pi}{5}$	$\frac{7\pi}{5}$	π	14	25	1	Y
36	50	1	$\frac{\pi}{5}$	$\frac{6\pi}{5}$	$\frac{\pi}{5}$	36	50	1	Y
27	20	1	$\frac{9\pi}{5}$	0	$\frac{8\pi}{5}$	27	20	1	Y

The search metric of Eq. 6.12 yielded the correct position estimate for noise free synthetic data.

Next, the synthetic data simulation was repeated with noise added to corrupt the receiver wand's data. Recall that the amplitude values computed via this simulation are analogous to the Mantenna Wand's data after the envelope detection stage, as described in Section 3.3.2, thus noise added to the synthetic data is analogous to the noise being added after the envelope detection stage in the Mantenna's DSP processing. White gaussian noise was added to the synthetic data and 10,000 simulations were run for each Signal to Noise Ratio (SNR) value. For each SNR value the error in position estimate for each iteration was tallied, and the total error was computed as the Root Mean Square (RMS) error of the ten-thousand runs at that SNR value. The results of this noise simulation are seen in Fig. 6.4.

Fig. 6.4 shows the RMS error for SNR values between 0dB and 2dB. From this, we see at 0dB the average position error is quite large, being over 30 feet of RMS error. As the SNR increases the average position error rapidly drops, and by the time the SNR is increased to $\approx$ 0.5dB the average position error is at 10 feet of RMS error. As the SNR approaches 1dB, the average error is well under 3 feet of RMS error, and as the SNR increases to 1.5dB we see the average error approaches 0 feet of RMS error.

The results show that the search metric used to obtain the position estimate algorithm is very robust as it is able to handle a very low SNR and still produce position estimates that are very close to the correct values. It is unrealistic to add noise to the signal after

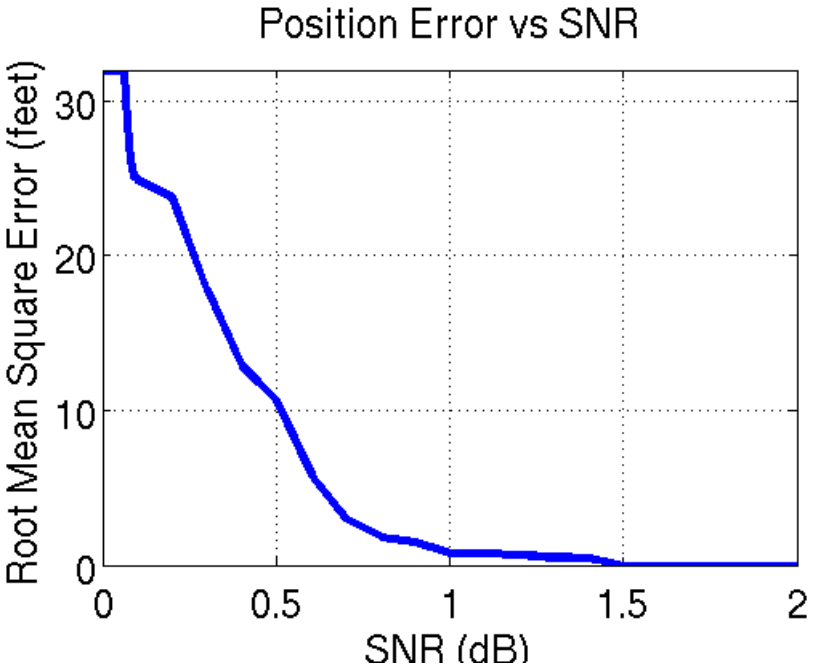

Figure 6.4: Position Error vs SNR

the envelope detector stage; in normal operation, any gaussian noise would be added in the environment (before the receiver antenna sense the signal, as per Section 3.3.1), and the low pass filtering and envelope detection stages of the DSP processing would eliminate most of the ill effects due to noise. Thus, adding the gaussian noise at the output of the envelope detector stage can only be viewed as a benchmark scenario for comparison of solution metrics and not an evaluation of complete receiver performance. Such an analysis is a prime candidate for future research.

The ability to tolerate low SNR will also simplify the implementation of a complete system since non-ideal components such as ADCs and finite precision DSP arithmetic will not significantly hinder the development of a Near Field based location system. Additionally, the performance of the system should increase with more receiver wands surrounding the building.

6.6 Alden Hall Simulation Results

The data captured in Summer 2008 at Alden Hall, detailed in Chapter 5, was then processed with the search algorithm. The Alden Hall data was used as the receiver data, with the synthetic data used to determine a position estimate. The 31 foot by 31 foot

quadrant of Alden Hall data was used to create a 62 foot by 62 foot grid of receiver points (with 1 foot increments, for a total of 3,844 points), and a 31 foot by 31 foot quadrant of synthetic data was used to generate a 62 foot by 62 foot grid of comparison points (with 0.1 foot increments, for a total of 385,641 points).

Before performing this simulation, one of the one datasets would need to be scaled in order to have the amplitudes match that of the other dataset since the received signal amplitude is not directly measured. The measured signal is a function of antenna Q, RF gain, mixer gain, etc. The technique used to scale the amplitudes is described in the following section.

6.6.1 Scaling Data via Arbitrary Point Normalization

The idea behind this method is simple. A random point is chosen from the Alden Data grid, the scale needed for parity with the synthetic data at that point is computed, then that scale is applied to the entire Alden Data grid. When testing this method, a simulation was executed where the arbitrary point was determined each time for each iteration of the simulation, the normalization computed and applied, and the position estimate calculated.

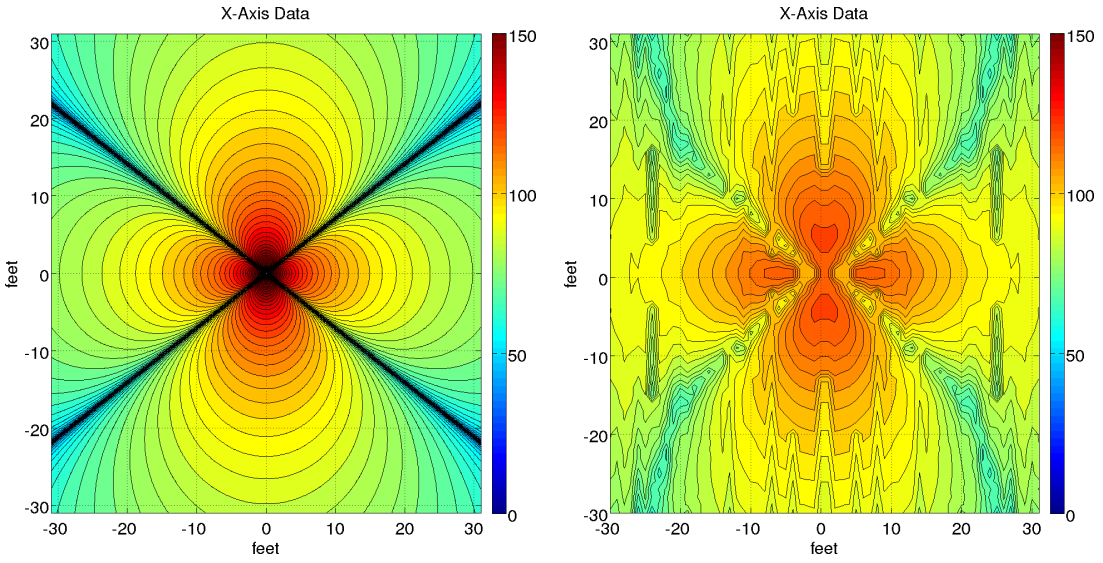

(a) $20\log_{10}|H|$ X-Axis Synthetic Data

(b) $20\log_{10}|H|$ X-Axis Alden Data

Figure 6.5: Antenna #1 X-Axis Signal Plots

Fig. 6.5 through Fig. 6.13 show a side by side comparison of the MATLAB Numerical Signal Function and the scaled Alden Hall Data. Figs. 6.5-6.7 show plots for the first antenna, Figs. 6.8-6.10 show plots for the second antenna, and Figs. 6.11-6.13 show

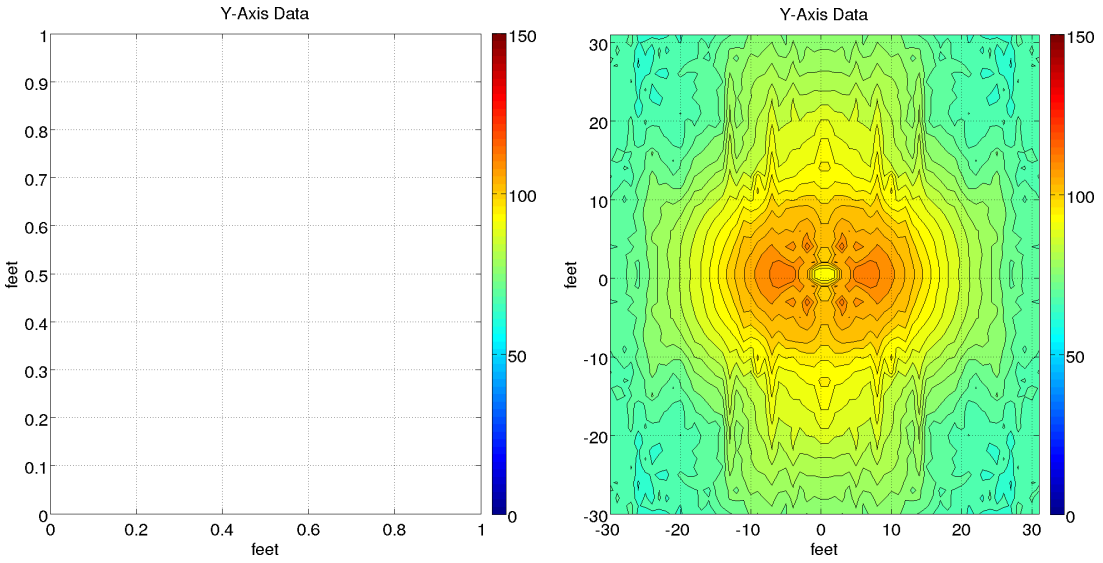

(a) $20\log_{10}|H|$ Y-Axis Synthetic Data (b) $20\log_{10}|H|$ Y-Axis Alden Data

Figure 6.6: Antenna #1 Y-Axis Signal Plots

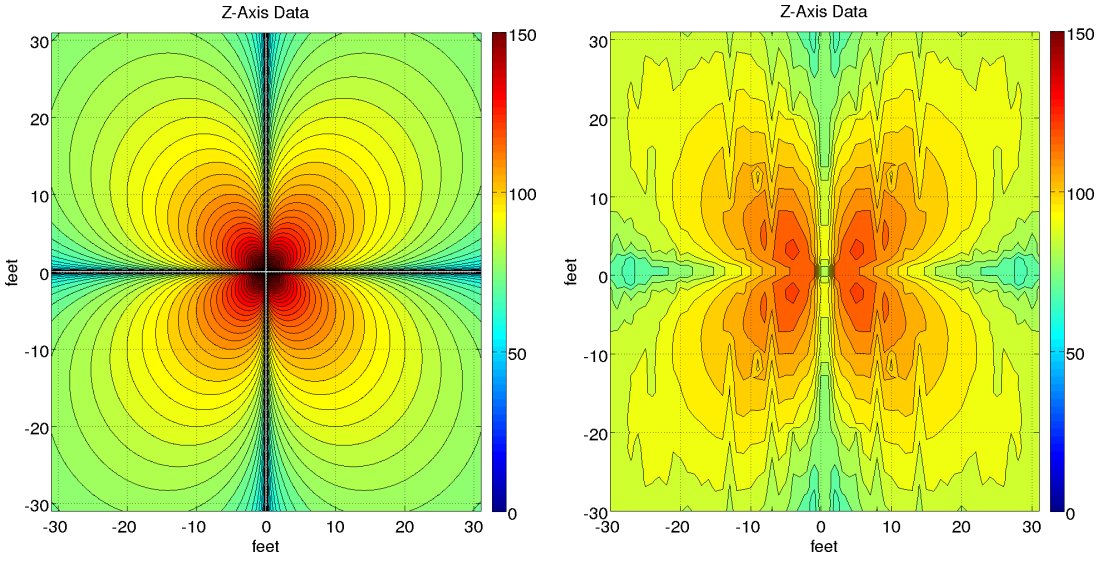

(a) $20\log_{10}|H|$ Z-Axis Synthetic Data (b) $20\log_{10}|H|$ Z-Axis Alden Data

Figure 6.7: Antenna #1 Z-Axis Signal Plots

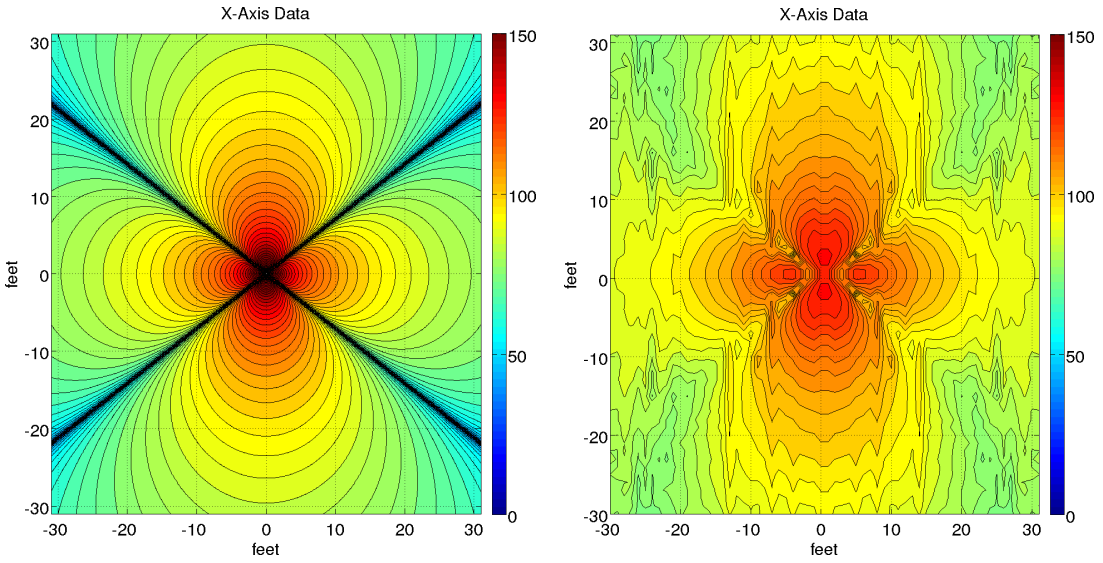

(a) $20\log_{10}|H|$ X-Axis Synthetic Data (b) $20\log_{10}|H|$ X-Axis Alden Data

Figure 6.8: Antenna #2 X-Axis Signal Plots

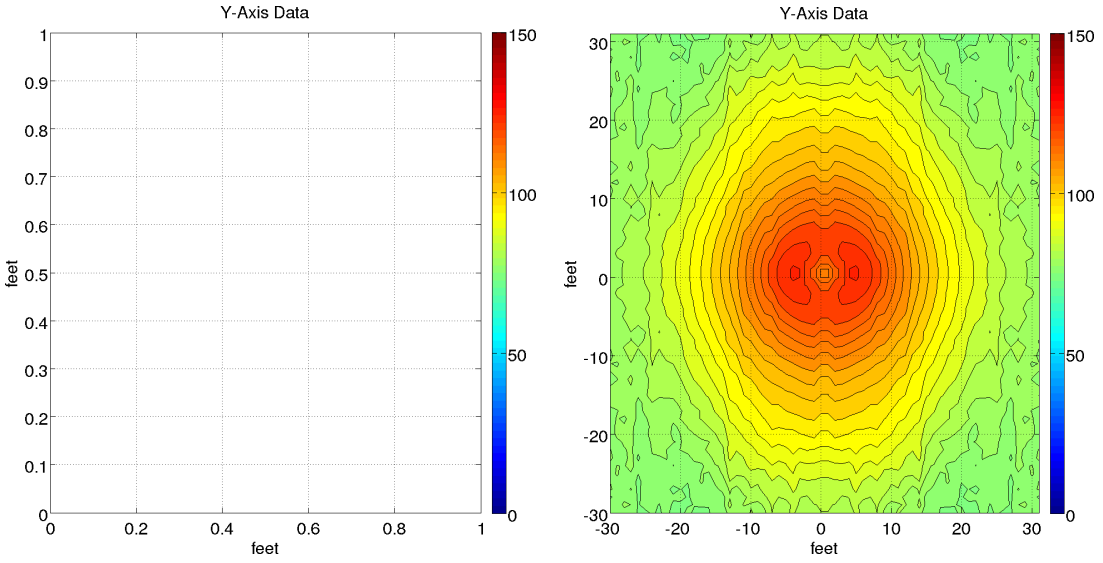

(a) $20\log_{10}|H|$ Y-Axis Synthetic Data (b) $20\log_{10}|H|$ Y-Axis Alden Data

Figure 6.9: Antenna #2 Y-Axis Signal Plots

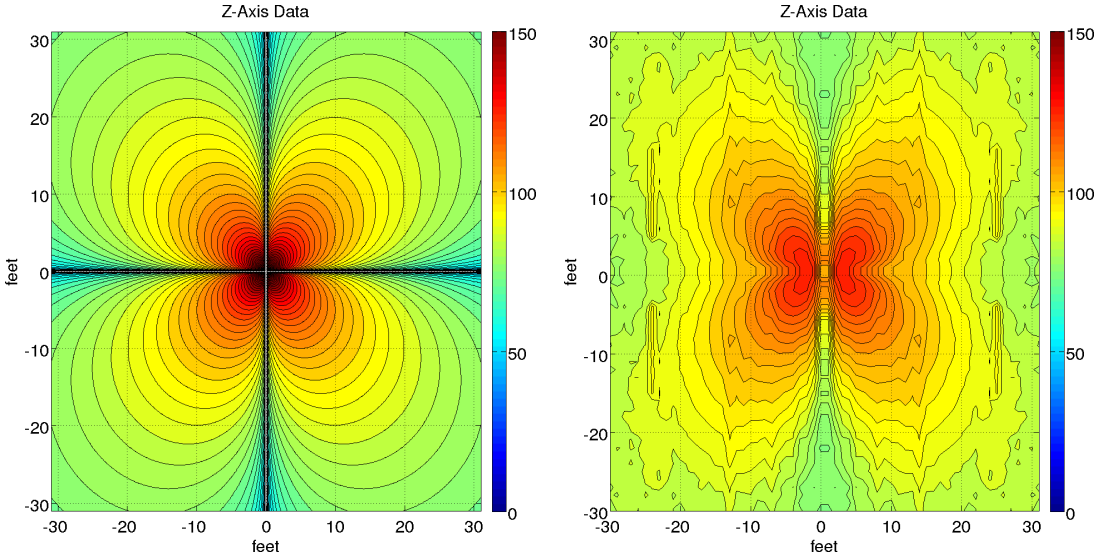

(a) $20\log_{10}|H|$ Z-Axis Synthetic Data (b) $20\log_{10}|H|$ Z-Axis Alden Data

Figure 6.10: Antenna #2 Z-Axis Signal Plots

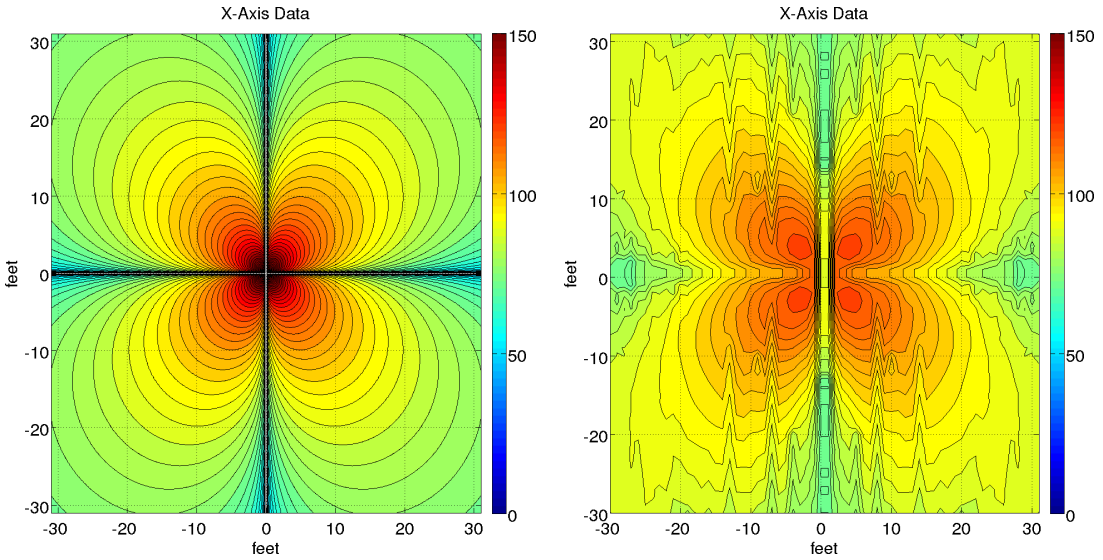

(a) $20\log_{10}|H|$ X-Axis Synthetic Data (b) $20\log_{10}|H|$ X-Axis Alden Data

Figure 6.11: Antenna #3 X-Axis Signal Plots

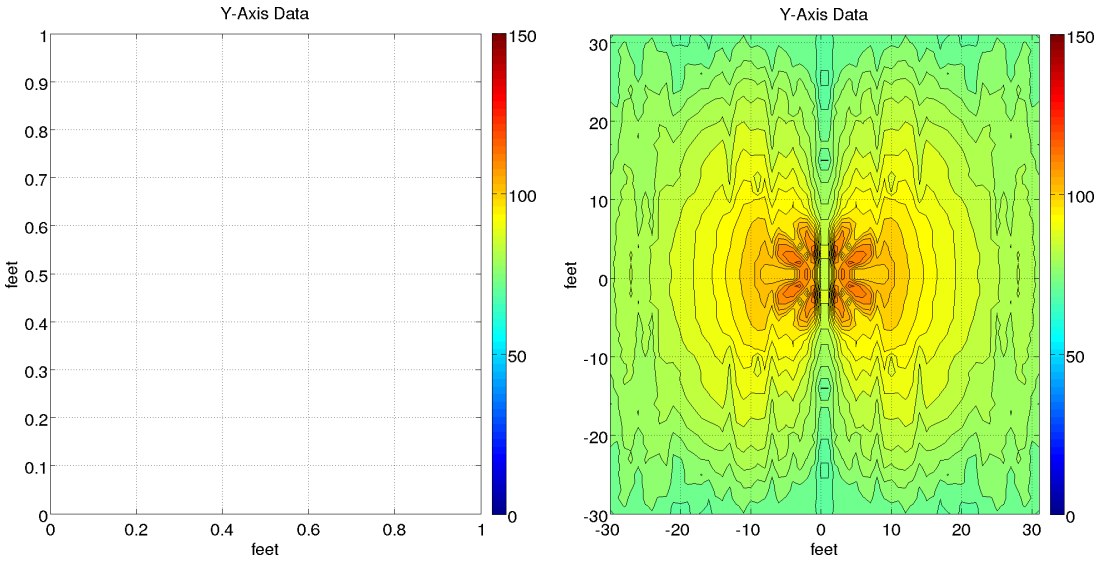

(a) $20\log_{10}|H|$ Y-Axis Synthetic Data (b) $20\log_{10}|H|$ Y-Axis Alden Data

Figure 6.12: Antenna #3 Y-Axis Signal Plots

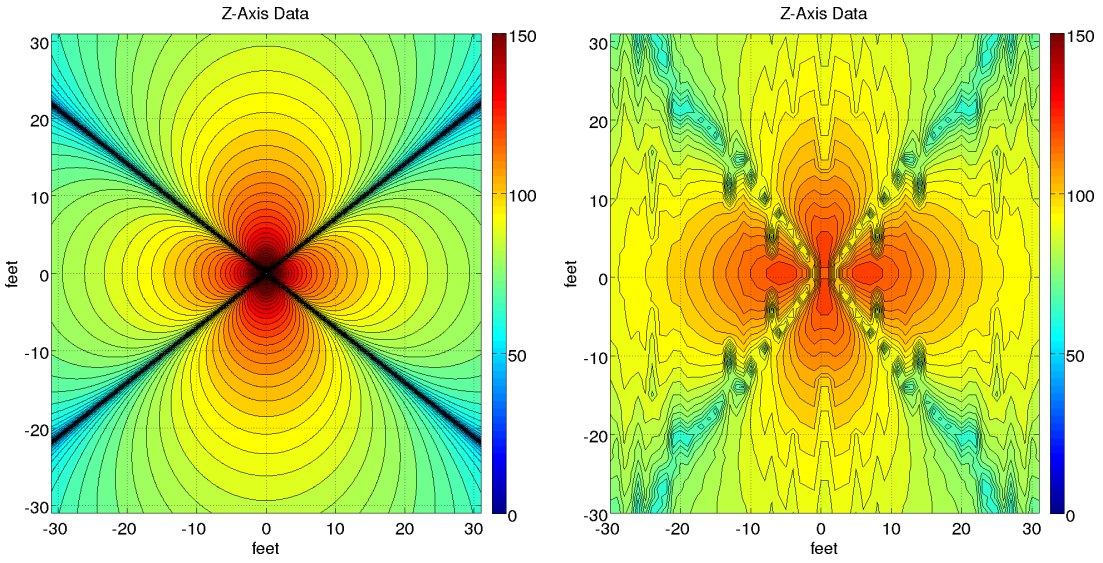

(a) $20\log_{10}|H|$ Z-Axis Synthetic Data (b) $20\log_{10}|H|$ Z-Axis Alden Data

Figure 6.13: Antenna #3 Z-Axis Signal Plots

plots for the third antenna. The images where signal function plots contain a null show the corresponding Alden Data containing some leakage, as per Figs. 6.6, 6.10, and 6.11. The remaining plots show the Alden Data's general shape is similar to the corresponding signal function plot, but is not as smooth; this is due in part to the coarseness of the spatial sampling and partly due to distortions of the field from metal structures in the building beneath the floor of the hall in which testing took place. Please refer to Table 3.1 for information indicating which antenna corresponds to which transmitter frequency component.

Due to all four quandrants being symmetrical, this simulation used one quadrant of the 62x62 foot grid. Fig. 6.14 shows the 31x31 foot quadrant of Signal Function data for the X-Axis of Antenna #1, and Fig. 6.15 shows the corresponding normalized Alden Hall data. Comparing Figs. 6.14-6.15 we see the Alden Hall data is quite distorted. Steel beams from the hallway one floor below are most likely ducting the signal in such a manner as to distort the signal as seen in Fig. 6.15. Additionally, the receiver's RF Amplifiers saturate when the transmitter is close to the receiver due to the high signal strength. This saturation is evident in the bottom left corner of Fig. 6.15 as the amplitude does not fall off as quickly as it should in the near field. The near field should drop by 18dB/octave. Far from the transmitter we see this behavior while up close one finds a drop off of only about 10dB/octave. This non-linearity is used to the Mantenna's advantage to detect when the transmitter is within a few feet from the receiver in the "saturation detection" stage described in Section 3.3.2. The important thing to take way from Figs. 6.14-6.15 is the Alden Data is somewhat distorted and thus the expectations for a correct position estimate are low. Section 6.6.2 shows the results of using the Normalized Alden Hall data as receiver data and computing the position estimate against the Signal Function.

6.6.2 Position Estimate Result

As described in Section 6.6.1, the Alden hall data was normalized to have the amplitudes match those of the Signal Function data. Additionally, the Alden Hall dataset was shown to be sufficiently distorted that an accurate position estimate is not expected.

Because of accumulating errors with increasing distance from the transmitter, only the inner 10x10 foot section of the grid is shown. The simulation was executed and the results are seen in Fig. 6.16. Fig. 6.16 depicts an error vector plot for the position estimate error at each point along a 10 foot by 10 foot grid of points starting at the origin. This region

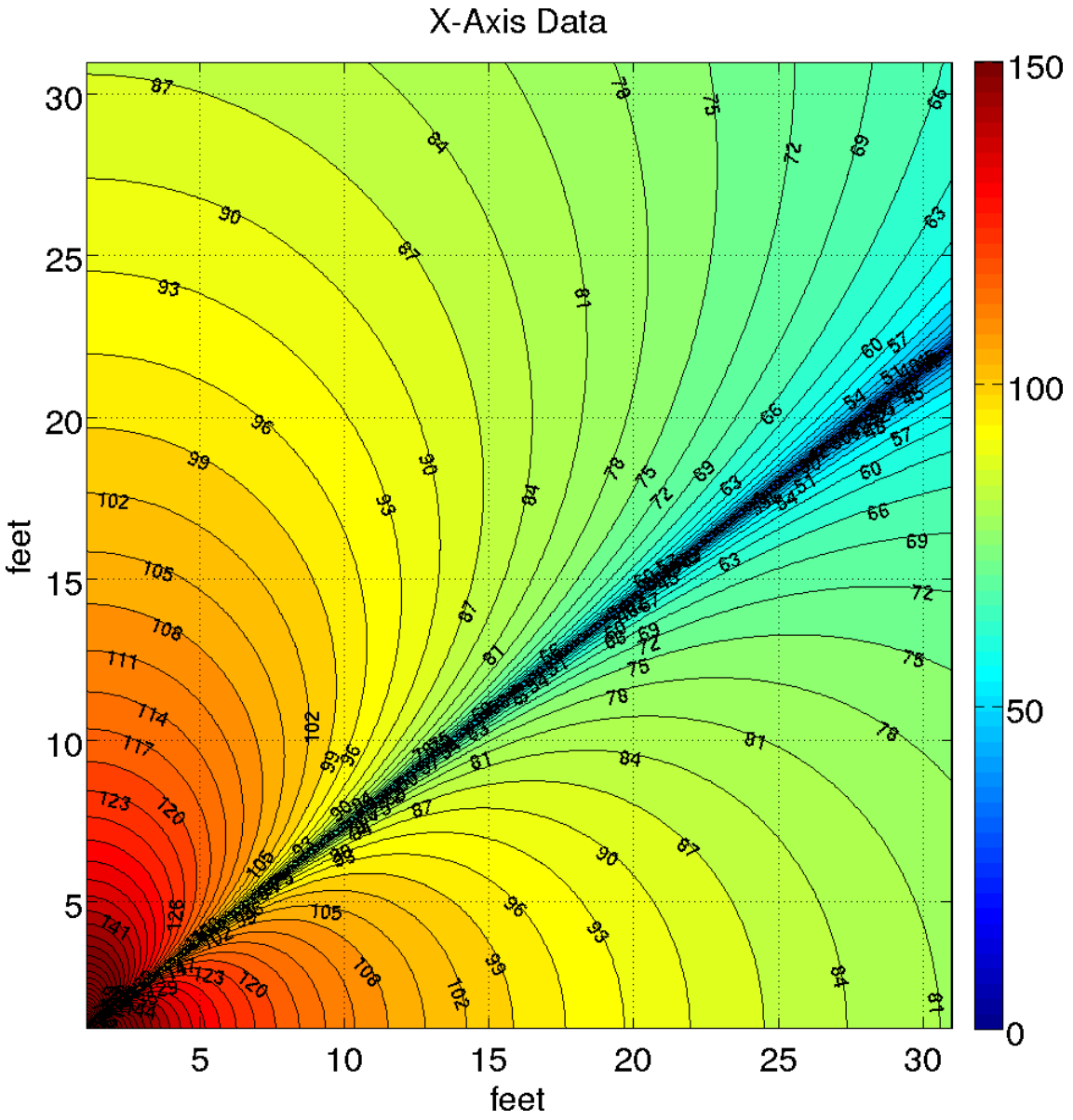

Figure 6.14: Simulated Data - Quandrant 1

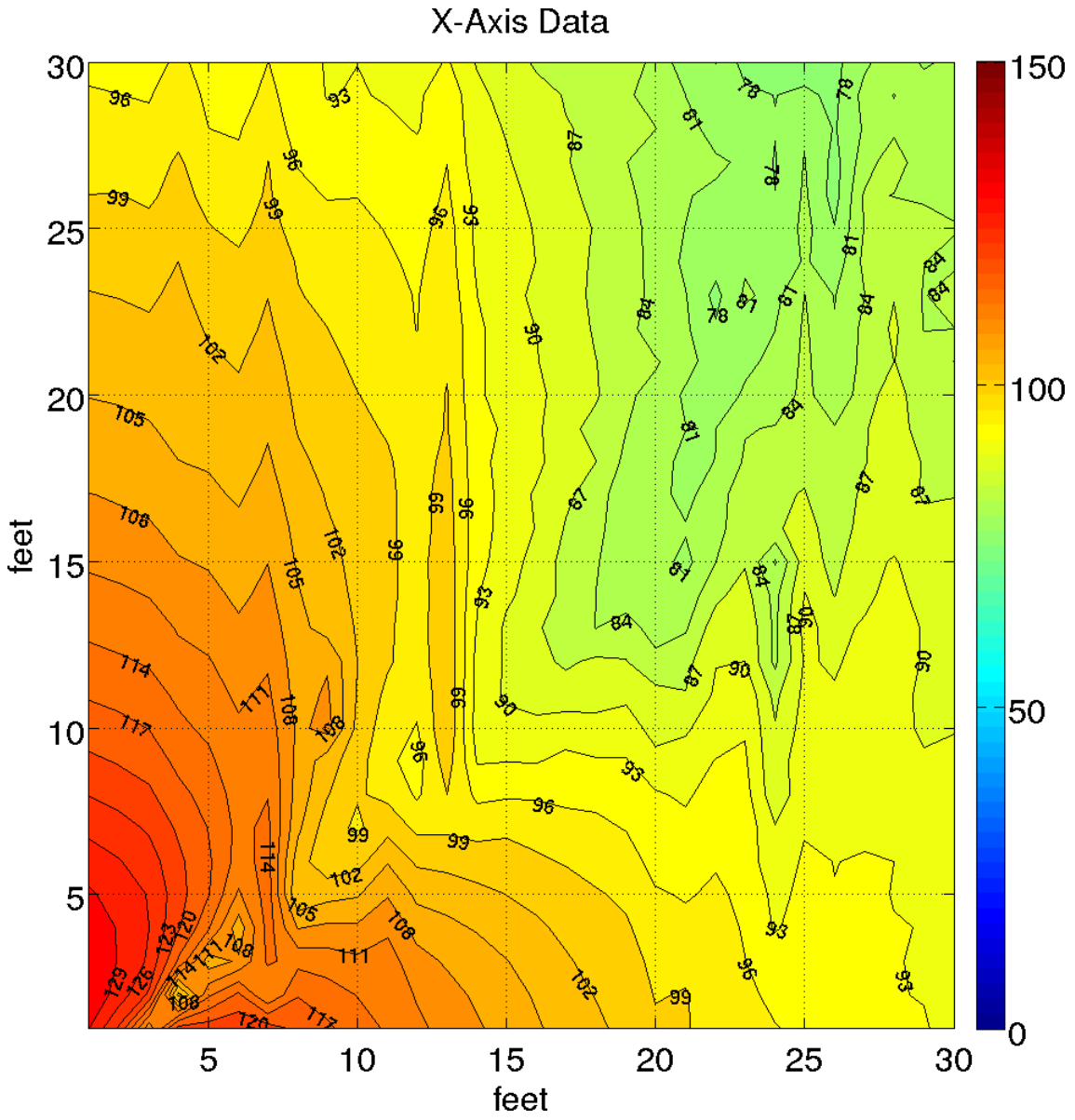

Figure 6.15: Normalized Alden Data - Quadrant 1

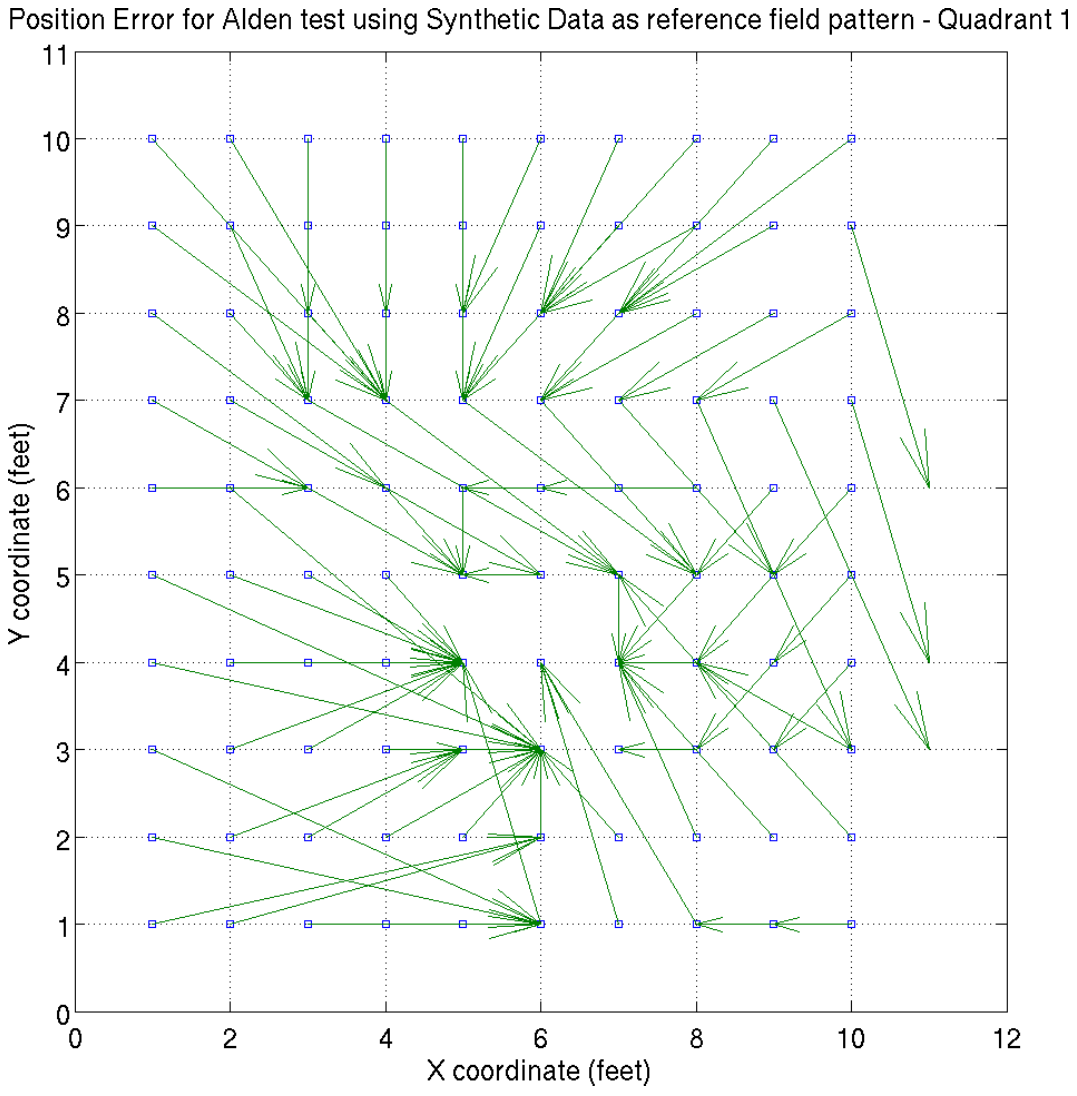

Figure 6.16: Position Error - Alden test using Synthetic Data as reference field pattern - Quadrant 1

has an RMS position error of 2.62 feet, which is surprisingly low. However, this error would be less with a less distorted data set.

The results shown in Fig. 6.16 show that Near Field Location is not usable in the minimal configuration of one receiver and one transmitter described by Section 5.1. However, the foundation has been lain for the multi-receiver wand solution.

Chapter 7

Conclusions

This thesis develops the theoretical background for a Near Field based Location System. The hardware is based upon the Mantenna Homing Wand, and the theoretical groundwork for a position tracking and rescue system with the hardware has been presented.

This thesis has documented the essential background information about the Mantenna project, including the test which motivated the idea of the Near Field Locator. Consequently, the new transmitter system was developed along with the research towards the goal of a Near Field Locator system.

The theory presented in this thesis begins by presenting the relevant electromagnetic background regarding the near field's shield penetration properties, the progresses on how to obtain the numerical simulation of the field amplitude function in any position in x-y and for any transmitter orientation. Subsequently, Section 6.3 provides a position estimation algorithm which is independent of the transmitter orientation and Section 6.5 demonstrates the ability of the position estimation algorithm to handle very noisy (low SNR) receiver data reliably.

In the final steps of this thesis, the Alden Hall data captured in June 2008 was used as receiver data and compared against the MATLAB numerical field values. As described in Section 6.6.2, real-world field distortions obviate the use of a single receiver wand and the foundation for a multi-receiver solution has been provided.

In addition, the author would like to present some future research ideas for further development of the Near Field Locator. These are outlined in the following sections.

7.1 Future Work

While this thesis has made contributions towards understanding the feasibility of the Near Field Locator idea; a real world system has yet to be implemented.

7.1.1 New Hardware

While the Mantenna Homing Wand hardware is great for the Homing Wand purposes and has served to aid the minimal configuration of the Near Field Locator idea, new receivers will need to be built to help facilitate non-minimal configuration Near Field Location testing and development. Multiple receiver wands will need to communicate their data to a central processing station. This processing station must have appropriately fast hardware to implement the position estimation and compute the position estimate in real-time.

7.1.2 Multi-Receiver Position Metric Algorithm

In addition to building new hardware for a non-minimal configuration test, the search metric must be improved to provide a position estimate from several receiver wands. The metric provided by Section 6.12 must be expanded to support determining a position estimate from multiple receiver wands. The use of multiple receivers will allow for a more robust system, as it would be less susceptible to noise and structurally induced variations of the field.

7.1.3 Near Field Locator Testing

After development of a non-minimal configuration NFL system, the performance evaluation of this configuration must be evaluated in real structures. A system test in various harsh RF environments should be performed to evaluate the performance of such a system. For example, an NFL test at Atwater Kent Laboratories at WPI should be performed to verify the NFL can perform in harsh RF environments where the PPL system fails.

7.1.4 Physiological Status Monitoring

In addition to pure location, the NFL could be developed further to pass physiological data to the incident commander via a separate communication channel. Items such as heart

rate, oxygen saturation, and respiration could be beneficial to the incident commander in determining which firefighters are near health related emergencies.

7.2 Implications

This thesis has put forth the theoretical foundations for a Near Field based position tracking and rescue system. Built upon technology demonstrated to work in harsh RF environments, the NFL could be used to more accurately and more reliably track firefighters and other emergency personnel inside harsh RF environments such as most commercial and industrial buildings.

The Near Field Location System is less plagued by multipath effects than high frequency systems, such as the PPL system. This thesis is one crucial step towards making a working, practical, and usable tracking and rescue system for firefighters a reality. It is my sincere hope this technology will be built upon and some day be in use, preventing another tragedy such as the Worcester Cold Storage fire from occurring.

Bibliography

[1] J. R. Anderson, "Abandoned Cold Storage Warehouse Multi-Firefighter Fatality Fire," U.S. Fire Administration, Tech. Rep. USFA-TR-134, December 1999, www.usfa.dhs.gov/downloads/pdf/publications/tr-134.pdf.

[2] District Chief John F. Sullivan, Personal Communication, Worcester Fire Department, December 7th 2007.

[3] J. Orr and D. Cyganski, "Firefighter and other Emergency Personnel Tracking and Location Technology for Incident Response," Worcester Polytechnic Institute, Tech. Rep., July 2001.

[4] G. Lachapelle, H. Kuusniemi, D. T. H. Dao, G. MacGougan, and M. E. Cannon, "HSGPS Signal Analysis and Performance under Various Indoor Conditions," University of Calgary, Tech. Rep., September 2003.

[5] Stephen Alsup, "Tracker FRT," EXIT Technologies, August 2006, Precision Indoor Personnel Location and Tracking for Emergency Responders Conference at Worcester Polytechnic Institute, August 2006, http://www.ece.wpi.edu/Research/PPL/Workshops/2006/PDF/ExitTech.pdf.

[6] *Avalanche beacon magnetic field calculations for rescue techniques improvement.* Geoscience and Remote Sensing Symposium, July 2007.

[7] V. Amendolare, "Synchronization in a Precision Indoor Location System," Master's thesis, Worcester Polytechnic Institute, 2007.

[8] J. R. Moser, "Low-Frequency Low-Impedance Electromagnetic Shielding," *IEEE Transactions on Electromagnetic Compatibility*, vol. 30, no. 3, pp. 202–210, August 1988.

[9] F. T. Ulaby, *Electromagnetics for Engineers.* Pearson Prentice Hall, 2005.

[10] C. A. Balanis, *Antenna Theory: Analysis and Design*, 3rd ed. Wiley, 2005.

[11] A. Nishikata and A. Sugiura, "Analysis for Electromagnetic Leakage through a Plane Shield with an Arbitrarily-Oriented Dipole Source," *IEEE Transactions on Electromagnetic Compatibility*, vol. 34, no. 1, February 1992.

[12] P. R. Bannister, "New Theoretical Expressions for Predicting Shielding Effectiveness for the Plane Shield Case," *IEEE Transactions on Electromagnetic Compatibility*, vol. EMC-10, no. 1, March 1968.

[13] H. A. Wheeler, "The Radiansphere Around a Small Antenna," in *Proceedings of the IRE*, 1957.

[14] E. C. Snelling, *Soft Ferrites: Properties and Applications.* CRC Press, 1969.

[15] R. DeVore and P. Bohley, "The Electrically Small Magnetically Loaded Multiturn Loop Antenna," *IEEE Transactions on Antennas and Propagation*, vol. AP-25, no. 4, pp. 496–505, July 1977.

[16] T. Simpson and Y. Zhu, "The Electrically Small MultiTurn Loop Antenna with a Spheroidal Core," *IEEE Antennas and Propagation Magazine*, vol. 48, no. 5, pp. 54–66, 2006.

[17] ——, "Correction to "The Electrically Small MultiTurn Loop Antenna with a Spheroidal Core," *IEEE Antennas and Propagation Magazine*, vol. 49, no. 2, pp. 80–81, 2007.

[18] J. B. Kuipers, *Quaternions and Rotation Sequences: A Primer with Applications to Orbits, Aerospace and Virtual Reality.* Princeton University Press, August 2002.

[19] G. H. Golub and C. F. Van Loan, *Matrix Computations*, 3rd ed. Johns Hopkins Univ. Press, 1996.

[20] S. Umeyama, "Least-Squares Estimation of Transformation Parameters Between Two Point Patterns," *IEEE Transactions on Pattern Analysis and Machine Intelligence*, vol. 13, no. 4, pp. 376–380, April 1991.